IMPROVEMENT AND COMPARISON OF COMPLEX B_1 MAPPING TECHNIQUES FOR USE IN MREPT

A THESIS SUBMITTED TO

THE GRADUATE SCHOOL OF ENGINEERING AND SCIENCE

OF BILKENT UNIVERSITY

IN PARTIAL FULFILLMENT OF THE REQUIREMENTS FOR

THE DEGREE OF

MASTER OF SCIENCE

IN

ELECTRICAL AND ELECTRONICS ENGINEERING

By

Safa Özdemir

September 2018

Improvement and comparison of complex B_1 mapping techniques for use in MREPT
By Safa Özdemir
September 2018

We certify that we have read this thesis and that in our opinion it is fully adequate, in scope and in quality, as a thesis for the degree of Master of Science.

Yusuf Ziya İder(Advisor)

Ergin Atalar

Behçet Murat Eyüboğlu

Approved for the Graduate School of Engineering and Science:

Ezhan Karaşan
Director of the Graduate School

ABSTRACT

IMPROVEMENT AND COMPARISON OF COMPLEX B_1 MAPPING TECHNIQUES FOR USE IN MREPT

Safa Özdemir
M.S. in Electrical and Electronics Engineering
Advisor: Yusuf Ziya İder
September 2018

Impedance imaging, (i.e., conductivity, σ, and permittivity, ϵ) provides helpful information about contrast between healthy and malignant tissues. As one of the impedance imaging techniques, Magnetic Resonance Electrical Properties Tomography (MREPT) uses the perturbation on B_1 caused by electrical properties, and via solving the inverse problem with the help of measured B_1 field, electrical properties are obtained. Therefore, to obtain conductivity using MREPT, the knowledge of B_1 phase and magnitude is required. This thesis focuses on improvement and comparison of complex B_1 mapping techniques for use in MREPT. In this manner, balanced steady-state free precession (bSSFP) imaging, which is one of the best candidates to obtain B_1 phase, is investigated. bSSFP imaging has high speed, high signal-to-noise ratio (SNR), motion insensitivity and automatic eddy current compensation. On the other hand, it suffers greatly from B_0 inhomogeneity and the concomitant "banding artifact". In regions of banding artifact, MR signal reduces significantly in magnitude, and also phase errors occur. The correction of phase errors is conducted by using three different techniques: Inserting B_0 and T_2 information, linearization for off-resonance estimation (LORE) algorithm, and PLANET method. In the next step, 2D version of phase-based convection-reaction equation based MREPT (phase-based cr-MREPT) technique is utilized to obtain conductivity maps from corrected phase images that are acquired from three aforementioned techniques. In order to verify the effects of correction techniques, an experimental agar-saline phantom with conductivity contrasts is constructed. It is shown that, for all phase correcting techniques, banding artifact is removed from phase images and accurate conductivity maps are obtained. Yet, inserting B_0 and T_2 information results in lengthy scanning time if both B_0 and T_2 information is acquired via traditional, reliable methods which are widely considered as golden truth. On the other hand, PLANET

method suffers from B_0 drift and propagation of error. Therefore, LORE algorithm is considered as the best candidate to obtain B_1 phase images which is required to find conductivity maps. Besides phase-based MREPT methods, there also exists MREPT methods that requires both B_1 phase and magnitude information. In the purpose of acquiring B_1 magnitude images, three different methods are investigated, namely double angle (DA) method, actual flip-angle imaging (AFI) method, and Bloch-Siegert shift (BSS) based method. To analyze B_1 magnitude mapping qualities of these methods, theoretical SNR calculations and phantom experiments are conducted. Both theoretical and experimental studies reveal that, based on SNR results, BSS based method is advantageous over AFI method and DA method. For each of B_1 magnitude mapping methods, conductivity maps are obtained. It is found that, although standard MREPT method is indifferent to the choice of B_1 magnitude mapping methods, high-SNR B_1 magnitude maps provide better conductivity results for standard cr-MREPT method.

Keywords: Magnetic Resonance Electrical Properties Tomography (MREPT), convection-reaction equation based MREPT (cr-MREPT), conductivity, bSSFP, banding artifact, phase-based, complex B_1 mapping.

ÖZET

MREÖT'TE KULLANIM AMACIYLA KARMAŞIK B_1 HARİTALAMA TEKNİKLERİNİN İYİLEŞTİRİLMESİ VE KARŞILAŞTIRILMASI

Safa Özdemir
Elektrik Elektronik Mühendisliği, Yüksek Lisans
Tez Danışmanı: Yusuf Ziya İder
Eylül 2018

Empedans görüntüleme (iletkenlik, σ ve elektriksel geçirgenlik, ϵ) sağlıklı ve habis dokular arasındaki kontrast hakkında yararlı bilgiler sağlar. Empedans görüntüleme tekniklerinden biri olan Manyetik Rezonans Elektriksel Özellik Tomografisi (MREÖT), elektriksel özelliklerin B_1 üzerinde yarattığı bozulmayı kullanır, ve elde edilen B_1 alanının yardımıyla ters problem çözülerek elektriksel özelikler elde edilir. Bu nedenle, MREÖT kullanarak iletkenlik elde etmek için B_1 faz ve genlik bilgisi gereklidir. Bu tez, MREÖT'te kullanım amacıyla karmaşık B_1 haritalama tekniklerinin iyileştirilmesi ve karşılaştırılması üzerine eğilmektedir. Bu bağlamda, B_1 fazını elde etmek için en iyi adaylardan birisi olan, dengeli kararlı durum serbest devinim (dKDSD) görüntülemesi araştırılmıştır. dKDSD görüntülemesi yüksek hıza, yüksek sinyal-gürültü oranına (SGO), harekete duyarsızlığa ve otomatik girdap akımları telafisine sahiptir. Öte yandan, B_0 homojensizliğinden ve buna eşlik eden "şerit artefaktı"ndan önemli ölçüde etkilenmektedir. Şerit artefaktının oluştuğu bölgelerde MR sinyali genlik olarak azalmakta ve aynı zamanda faz hataları ortaya çıkmaktadır. Faz hatalarının düzeltilmesi üç farklı teknikle gerçekleştirilmektedir: B_0 ve T_2 bilgisini kullanma, rezonans dışı kestirim için doğrusallaştırma (RDKD) algoritması ve PLANET yöntemi. Sonraki adımda, bahsedilen üç teknikten elde edilen düzeltilmiş faz görüntülerinden iletkenlik haritalarını elde etmek için faz temelli konveksiyon-reaksiyon denklemi temelli MREÖT (faz temelli kr-MREÖT) tekniğin 2B versiyonu kullanılmakadır. Düzeltme tekniklerinin etkilerini doğrulamak için, iletkenlik kontrastlı, deneysel agar-tuzlu su fantomu hazırlanmıştır. Tüm faz düzeltme teknikleri için şerit artefaktının faz görüntülerinden temizlendiği ve doğru iletkenlik haritalarının elde edildiği gösterilmiştir. Ancak, B_0 ve T_2 bilgisi, doğruluğu kabul edilen geleneksel ve güvenilir teknikler aracılığıyla elde edildiğinde, B_0

ve T_2 bilgisini kullanma uzun tarama süresiyle sonuçlanmaktadır. Diğer yandan, PLANET yöntemi B_0 sürüklenmesi ve hatanın yayılmasından etkilenmektedir. Bu nedenle, RDKD algoritması iletkenlik haritalarını bulmak için gerekli olan B_1 faz görüntülerini elde etmek için en iyi aday olarak düşünülmektedir. Faz temelli MREÖT yöntemlerinin yanında, B_1 fazı ve genliği bilgisine ihtiyaç duyan MREÖT yöntemleri de bulunmaktadır. B_1 genlik görüntülerini elde etmek amacıyla, üç farklı yöntem araştırılmıştır: çift açı (ÇA) yöntemi, asıl döndürme-açı görüntüleme (ADG) yöntemi ve Bloch-Siegert kayması (BSK) temelli yöntem. Bu yöntemlerin B_1 genlik haritalandırma yöntemlerinin kalitelerini analiz etmek için kuramsal SGO hesaplamaları ve fantom deneyleri gerçekleştirilmiştir. Kuramsal ve deneysel çalışmaların gösterdiği üzere, BSK temelli yöntem SGO açısından ADG yöntemi ve ÇA yöntemine göre avantajlıdır. Her bir B_1 genlik haritalandırma yöntemi için iletkenlik haritaları elde edilmiştir. Standart MREÖT yönteminin B_1 genlik haritalandırma yönteminin seçiminden etkilenmemesine rağmen, yüksek SGO değerli B_1 genlik haritaları standart kr-MREÖT yöntemi için daha iyi iletkenlik sonuçları sağlamaktadır.

Anahtar sözcükler: Manyetik Rezonans Elektriksel Özellik Tomografisi (MREÖT), konveksion-reaksiyon denklemi temelli MREÖT (kr-MREÖT), iletkenlik, dKDSD, şerit artefaktı, faz-temelli, karmaşık B_1 haritalaması.

Acknowledgement

It is difficult to overstate my gratitude to my supervisor, Prof. Yusuf Ziya İder. I am always inspired by his determination, wide range of knowledge, and dedication to the scientific progress. I am really indebted for his guidance in academic field and advices in real life situations. It has been an honor working with him.

I would like to thank Prof. Ergin Atalar and Prof. Behçet Murat Eyüboğlu for kindly accepting to be my jury members.

I also acknowledge The Scientific and Technological Research Council of Turkey (TÜBİTAK) for providing financial support, under the project code 114E522.

I also thank Volkan Açıkel, Umut Gündoğdu, Berk Silemek and Uğur Yılmaz, for answering my endless questions about MRI with great patience and helping me in my experiments. I also thank Aydan Ercingöz for giving me great advices when I need them. I also would like to express my sincere gratitude to Sevgi Gökçe Kafalı and Gülşah Yıldız, for cheering me up and helping me to get through hardships. For the great office environment, I want to thank my office mates, Çelik Boğa, Gökhan Arıtürk, Yiğit Tuncel, and Toygun Başaklar.

I cannot thank enough my friends, Eren Can Kovan, Selin Özbek, Mustafa Şimşek, Osman Fatih Kılıç, Sinan Mutlu, Sami Şimşekli, and Hüseyin Selvi. They have been on my side during my happy and difficult days. Their endless support and great advices helped me to continue.

Lastly, I owe my gratitude to my parents, who supported me every time I need. I am really lucky to have them.

Contents

List of Figures

Chapter 1

Introduction

Magnetic Resonance Imaging (MRI) is a well established diagnostic tool in medicine since 1980s. Main reasons of this are MRI operates in a non-invasive fashion and it does not use damaging ionizing radiation. In addition to these advantages, MRI provides plenty of contrast mechanisms by simply adjusting imaging parameters. The widely used contrast mechanisms are spin density (ρ) and relaxation times (T_1 and T_2). There are also clinically established contrast mechanisms such as flow, diffusion, magnetic susceptibility, and stiffness. This thesis focuses on one of the contrast mechanisms, which is electrical properties. Previously, it has been proven that electrical property imaging is a useful diagnostic tool, as it provides distinction between healthy and malignant tissues.

In the following section, uses of the electrical properties and different electrical property imaging techniques will be discussed. This will be followed by the objective and scope of the thesis. In the end, organization of the thesis will be given.

1.1 Electrical Property Imaging

Electrical property imaging aims at reconstructing conductivity, σ and permittivity, ϵ, of the tissues. Clinically, this information can be used to differentiate healthy and malignant tissues [1, 2]. Electrical property imaging is also used for transcranial magnetic stimulation [3], hyperthermia treatment [4], radiofrequency (RF) ablation [5], and calculating specific absorption rate (SAR) [6].

Earlier methods of impedance imaging are electrical impedance tomography (EIT) [7, 8] and magnetic induction tomography (MIT) [9] which are used to induce currents in the object by using either surface electrodes (EIT) or external coils (MIT). However, these methods yield images that have low spatial resolution in interior regions because the measurements, namely surface potentials, are not very sensitive to electrical property perturbations relatively far from the surface. To overcome this weakness, magnetic resonance electrical impedance tomography (MREIT) has been introduced [10–15]. In MREIT, current is induced by using surface electrodes in the frequency range of 10 Hz - 10 kHz and the resulting magnetic field is measured by MRI to reconstruct the image of electrical properties. Still, reducing the external applied current to below safety limits while having sufficient resolution is a problem in MREIT. A more recent method, magnetic resonance electrical properties tomography (MREPT), attempts to image electrical properties by measuring the magnetic field of currents induced at the Larmor frequency of the MRI system. MREPT is first suggested, in concept, by Haacke in 1991 [16], successfully applied for the first time by Wen in 2003 [17] and systematic research on MREPT is started by Katscher in 2009 [6].

In literature, widely-used formulation to describe relationship between clockwise rotating component of the transmit RF magnetic flux density, B_1^+ and admittivity ($\gamma = \sigma + i\omega\epsilon$) of the object is as follows [18]:

$$\gamma = \frac{\nabla^2 B_1^+}{i\omega\mu_0 B_1^+} \tag{1.1}$$

where ω is the Larmor frequency, μ_0 is permeability constant. Although Equation 1.1 is widely used for obtaining electrical property images, this method is

prone to noise and assumes locally constant electrical properties. Latter is also known as "local homogeneity assumption" (LHA), and causes boundary artifacts in conductivity maps. To solve this issue, as also reviewed in [18, 19], several approaches are followed [20–22]. As being one of them, Hafalir's approach introduced the convection-reaction partial differential equation (PDE) based method (cr-MREPT) [20].

For aforementioned methods, both the phase and the magnitude of B_1^+ are to be measured. Lately, phase-based methods, which do not depend on B_1^+ magnitude, are emerged. Standard phase based approach uses the equation:

$$\sigma(x, y) = \frac{\nabla^2 \phi(x, y)}{2\mu_0 \omega} \tag{1.2}$$

to find conductivity where ϕ is the transceive phase (if transmit phase is used, the factor 2 in the denominator is omitted) [23]. Yet, this method still suffers from boundary artifact because of LHA. Recently, a phase-based EPT method which does not require LHA is introduced by Gurler [24]. Gurler's method is similar in concept to Hafalir's method, but uses only the phase of B_1^+.

1.2 Objective and Scope of the Thesis

Equation 1.1 shows that to acquire admittivity, one needs both B_1 phase and magnitude.

To obtain phase, any MRI sequence that provides B_1^+ phase can be used. Among them, balanced steady state free precession (bSSFP) is favourable to obtain phase images since it has high speed, high SNR, motion insensitivity and automatic eddy current compensation due to balanced gradients [19, 25]. On the other hand, it suffers greatly from B_0 inhomogeneity and the concomitant "banding artifact". In regions of banding artifact, MR signal reduces significantly and also phase errors occur. Three different methods are used to obtain B_1 phase via bSSFP sequence. First method, which makes use of B_0 and T_2 maps, and two bSSFP runs with an excitation frequency difference is developed

to correct the phase distribution. By inserting B_0 and T_2 information into the steady state bSSFP complex signal equation, bSSFP phase images are corrected. Second method, linearization for off-resonance estimation - Gauss-Newton nonlinear search (LORE-GN) algorithm, involves general and fast two-step algorithm to estimate the unknowns in the steady state bSSFP signal equation by making use of multiple phase-cycled acquisitions [28]. First step involves converting the non-linear problem into a linear one by changing parameters in the steady state bSSFP signal equation. Then, to minimize non-linear least squares criterion, Gauss-Newton algorithm is applied. Third method, PLANET method, uses elliptical signal model to fit multiple phase-cycled bSSFP acquisition to ellipse [29]. By using center and semi-axes information of the ellipse, B_0, T_1, T_2 and RF phase information can be obtained. In this thesis, those three methods are implemented and their eligibility for MREPT is discussed.

To obtain magnitude, there are several well-established methods that can be used and need to be compared. First method is double-angle method which makes use of two different gradient-echo sequence with different flip angles, usually one of which is twice as much as the other [30]. From the pixel-wise ratio of two images, flip angle can be obtained. Second method, called actual flip-angle imaging (AFI) method utilizes gradient-echo sequence with two different repetition time (TR) [31]. Two TRs and the pixel-wise ratio of the two images are used to obtain flip angle. Lastly, Bloch-Siegert shift (BSS) based method uses additional RF pulse that has off-frequency with the spin resonance [32]. Precession angle gives B_1 magnitude information. In this thesis, those three methods are compared with respect to SNR values of B_1 maps and their availability for MREPT is discussed.

1.3 Organization of the Thesis

This thesis consists of five chapters.

Chapter 2 presents the theoretical background of conventional MREPT first. Formulation and limitations of standard MREPT method is discussed. After that,

formulation of the cr-MREPT method is given. Later, theory of conventional phase-based MREPT method is given with derivations and limitations. Lastly, formulation of phase-based cr-MREPT method is given.

Chapter 3 presents the methods for obtaining B_1 phase via bSSFP images. First, theory of steady state formulation of bSSFP is given. Then, each bSSFP phase correction method is introduced. Experimental results of those methods, namely transceive phases and conductivity maps from those transceive phases are given.

Chapter 4 presents the different B_1 magnitude mapping methods. For each method; theory, SNR calculation, experimental methods and results are given. Those methods are also compared with respect to their SNR values.

Chapter 5 presents the summary of both B_1 phase and magnitude methods. Also possible future directions are discussed.

Chapter 2

Theoretical Background for Magnetic Resonance Electrical Properties Tomography (MREPT)

2.1 Formulation and Limitation of Standard MREPT Method

From Maxwell's equations, the relationship between the clockwise (left-handed) rotating component of the transmit RF magnetic flux density, B_1^+, and admittivity of the object, γ can be derived as follows [18]:

$$-\nabla^2 B_1^+ = \frac{\nabla\gamma}{\gamma} \times (\nabla \times B_1^+) - i\omega\mu_0\gamma B_1^+ \tag{2.1}$$

With the assumption of locally constant electrical properties, known as "local homogeneity assumption" (LHA), the gradient term $\left(\frac{\nabla\gamma}{\gamma} \times (\nabla \times B_1^+)\right)$ is eliminated and admittivity becomes:

$$\gamma = \frac{\nabla^2 B_1^+}{i\omega\mu_0 B_1^+} \tag{2.2}$$

Although Equation 2.2 is widely used for obtaining electrical property images, this method suffers greatly from boundary artifacts, because of the elimination of the gradient term in Equation 2.1. To avoid this artifacts, several approaches were made. Hafalir [20] introduces convection-reaction partial differential equation based method. This method is in fact the solution of Equation 2.1 using numerical techniques. Liu's approach uses similar formulation in their method called "gradient based electrical properties tomography" [21]. In this method, with the knowledge of B_1^+, that is obtained by using a multi-channel transceiver coil, gradient of the electrical properties is obtained. Through spatial integration starting from a seed-point, both conductivity and permittivity are obtained. Contrast Source Inversion based EPT (CSI-EPT) views the object as a scatterer placed in the field generated by the RF coil [4]. EPs are updated until the measured field matches closely the field calculated by the solution of the integral-equation-based forward problem expressing the magnetic field as a function of the EPs.

For the aforementioned methods, both the phase and magnitude of B_1^+ are to be measured. Although there are well-established techniques to obtain the magnitude of B_1^+ [30–32], phase of B_1^+ cannot be measured directly in MRI. For birdcage-like quadrature volume coil configurations, transmit phase is roughly taken as half of the transceive phase. This widely used approach is called "transceive phase approximation", abbreviated as TPA [18, 23].

2.2 Formulation of Convection-Reaction Equation based MREPT (cr-MREPT) Method

Using μH^+ instead of B_1^+, x and y components of Equation 2.1 becomes:

$$\begin{aligned} -\nabla^2 H_x &= \frac{1}{\gamma}\left[\frac{\partial \gamma}{\partial y}\left(\frac{\partial H_y}{\partial x} - \frac{\partial H_x}{\partial y}\right) - \frac{\partial \gamma}{\partial z}\left(\frac{\partial H_x}{\partial z} - \frac{\partial H_z}{\partial x}\right)\right] \\ -\nabla^2 H_y &= \frac{1}{\gamma}\left[\frac{\partial \gamma}{\partial z}\left(\frac{\partial H_z}{\partial y} - \frac{\partial H_y}{\partial z}\right) - \frac{\partial \gamma}{\partial x}\left(\frac{\partial H_y}{\partial x} - \frac{\partial H_x}{\partial y}\right)\right] \end{aligned} \tag{2.3}$$

Then, calculating $-\nabla^2 H_x - i\nabla^2 H_y$ which is equal to $-2\nabla^2 H^+$, we obtain:

$$\begin{aligned} -2\nabla^2 H^+ = &-\frac{1}{\gamma}\frac{\partial\gamma}{\partial x} i\left(\frac{\partial H_y}{\partial x} - \frac{\partial H_x}{\partial y}\right) - \frac{1}{\gamma}\frac{\partial\gamma}{\partial y}\left(-\frac{\partial H_y}{\partial x} + \frac{\partial H_x}{\partial y}\right) \\ &- \frac{1}{\gamma}\frac{\partial\gamma}{\partial z}\left[2\frac{\partial H^+}{\partial z} - \frac{\partial H_z}{\partial x} - i\frac{\partial H_z}{\partial y}\right] - 2i\mu_0\gamma H^+ \end{aligned} \tag{2.4}$$

Using the definition of H^+ and $\nabla \cdot \mathbf{H} = 0$, $\left(\frac{\partial H_y}{\partial x} - \frac{\partial H_x}{\partial y}\right)$ becomes:

$$\begin{aligned} \frac{\partial H_y}{\partial x} - \frac{\partial H_x}{\partial y} &= \frac{\partial H_y}{\partial x} - \frac{\partial H_x}{\partial y} - i\left(\frac{\partial H_x}{\partial x} + \frac{\partial H_y}{\partial y} + \frac{\partial H_z}{\partial z}\right) \\ &= -2i\left(\frac{\partial H^+}{\partial x} - i\frac{\partial H^+}{\partial y} + \frac{1}{2}\frac{\partial H_z}{\partial z}\right) \end{aligned} \tag{2.5}$$

Using Equation 2.5, Equation 2.4 becomes:

$$\begin{aligned} \nabla^2 H^+ = &-\frac{1}{\gamma}\frac{\partial\gamma}{\partial x}\left(\left(\frac{\partial H^+}{\partial x} - i\frac{\partial H^+}{\partial y}\right) + \frac{1}{2}\frac{\partial H_z}{\partial z}\right) \\ &- \frac{1}{\gamma}\frac{\partial\gamma}{\partial y}\left(i\left(\frac{\partial H^+}{\partial x} - i\frac{\partial H^+}{\partial y}\right) + \frac{i}{2}\frac{\partial H_z}{\partial z}\right) \\ &- \frac{1}{\gamma}\frac{\partial\gamma}{\partial z}\left[\frac{\partial H^+}{\partial z} - \frac{1}{2}\frac{\partial H_z}{\partial x} - \frac{i}{2}\frac{\partial H_z}{\partial y}\right] - i\omega\mu_0\gamma H^+ \end{aligned} \tag{2.6}$$

Multiplying Equation 2.6 with u which is $1/\gamma$:

$$\boldsymbol{\beta} \cdot \nabla u + \nabla^2 H^+ u - i\omega\mu_0 H^+ = 0 \tag{2.7}$$

where

$$\begin{aligned} \nabla u &= \begin{bmatrix} \frac{\partial u}{\partial x} \\ \frac{\partial u}{\partial y} \\ \frac{\partial u}{\partial z} \end{bmatrix} = \begin{bmatrix} \frac{1}{\gamma^2}\frac{\partial\gamma}{\partial x} \\ \frac{1}{\gamma^2}\frac{\partial\gamma}{\partial y} \\ \frac{1}{\gamma^2}\frac{\partial\gamma}{\partial z} \end{bmatrix} \\ \boldsymbol{\beta} &= \begin{bmatrix} \frac{\partial H^+}{\partial x} - i\frac{\partial H^+}{\partial y} + \frac{1}{2}\frac{\partial H_z}{H_z} \\ i\frac{\partial H^+}{\partial x} - \frac{\partial H^+}{\partial y} + \frac{i}{2}\frac{\partial H_z}{H_z} \\ \frac{\partial H^+}{\partial z} - \frac{1}{2}\frac{\partial H_z}{\partial x} - \frac{i}{2}\frac{\partial H_z}{\partial y} \end{bmatrix} \end{aligned} \tag{2.8}$$

Assuming H_z is zero (valid for central regions for a birdcage RF coil) and $\frac{\partial u}{\partial z}$ is negligible, 2-D version of Equation 2.7 can be written as:

$$\mathbf{F} \cdot \overline{\nabla} u + \overline{\nabla}^2 H^+ u - i\omega\mu_0 H^+ = 0 \tag{2.9}$$

where

$$\overline{\nabla} u = \begin{bmatrix} \frac{\partial u}{\partial x} \\ \frac{\partial u}{\partial y} \end{bmatrix} \mathbf{F} = \begin{bmatrix} \frac{\partial H^+}{\partial x} - i\frac{\partial H^+}{\partial y} \\ i\frac{\partial H^+}{\partial x} - \frac{\partial H^+}{\partial y} \end{bmatrix} \tag{2.10}$$

2.3 Formulation and Limitations Standard Phase-Based MREPT Method

Recently, phase-based methods, which are solely based on B_1^+ phase rather than complex B_1^+, have emerged [26, 33]. Because of the difficulties in obtaining high SNR for the B_1^+ magnitude maps in a reasonable time, phase based methods offer an advantage especially for practical clinical applications. These methods are inherently free from TPA and do not require B_1^+ magnitude mapping [23]. By using LHA, from the Maxwell equations, the relationship between rotating component of the transmit magnetic flux density, B_1^+, and local complex wave number, k, can be written as:

$$\nabla^2 B_1^+ + k^2 B_1^+ = 0 \tag{2.11}$$

or in other form:

$$-k^2 = \frac{\nabla^2 B_1^+}{B_1^+} \tag{2.12}$$

where $k^2 = \mu_0 \varepsilon \omega^2 - i\mu_0 \sigma \omega$, μ_0 is the permeability constant, ε is the permittivity, σ is the conductivity and ω is the angular frequency. Since only the imaginary part of k^2 is related to the conductivity:

$$\mathrm{Im}(-k^2) = \mu_0 \sigma \omega = \mathrm{Im}\left(\frac{\nabla^2 B_1^+}{B_1^+}\right) \tag{2.13}$$

Then,

$$\sigma = \frac{1}{\mu_0 \omega}(\nabla^2 \phi^+ + \nabla \ln(\nabla B_1^+)) \tag{2.14}$$

Similar to standard MREPT formulation, by using LHA one can remove the term $(\ln(\nabla B_1^+))$ conductivity can be found as:

$$\sigma = \frac{\nabla^2 \phi^+}{\mu_0 \omega} \tag{2.15}$$

If transceive phase is used, Equation 2.15 becomes:

$$\sigma = \frac{\nabla^2 \phi^+}{2\mu_0 \omega} \tag{2.16}$$

Although this "standard" phase based formulation is free from TPA and does not require B_1^+ mapping, it assumes low B_1^+ magnitude gradients, in addition

to using LHA. While LHA causes well-known tissue-boundary artifacts in the conductivity images as mentioned before, assuming low B_1^+ magnitude gradient causes errors in the reconstructed conductivity values (up to 10% for 3T systems [23]) especially towards the boundary of the imaged object [27]. Recently, a phase-based EPT method which does not require LHA, but still assumes low B_1^+ gradients, is introduced by Gurler [24]. With Gurler's approach, called "phase-based cr-MREPT technique", boundary artifacts in the conductivity images are significantly reduced.

2.4 Formulation of Phase-Based cr-MREPT Method

cr-MREPT formulation can be written as:

$$\boldsymbol{\beta}^{\pm} \cdot \nabla \ln(\gamma) - \nabla^2 B_1^{\pm} + i\omega\mu\gamma B_1^{\pm} = 0 \tag{2.17}$$

where

$$\begin{aligned} \gamma &= \sigma + i\omega\varepsilon, \\ \nabla \ln(\gamma) &= \begin{bmatrix} \frac{\partial \ln(\gamma)}{\partial x} \\ \frac{\partial \ln(\gamma)}{\partial y} \\ \frac{\partial \ln(\gamma)}{\partial z} \end{bmatrix} \\ \boldsymbol{\beta}^{\pm} &= \begin{bmatrix} \beta_x^{\pm} \\ \beta_y^{\pm} \\ \beta_z^{\pm} \end{bmatrix} = \begin{bmatrix} \frac{\partial B_1^{\pm}}{\partial x} \mp i\frac{\partial B_1^{\pm}}{\partial y} + \frac{1}{2}\frac{\partial B_z}{\partial z} \\ \pm i\frac{\partial B_1^{\pm}}{\partial x} + \frac{\partial B_1^{\pm}}{\partial y} \pm i\frac{1}{2}\frac{\partial B_z}{\partial z} \\ -\frac{1}{2}\frac{\partial B_z}{\partial x} \mp i\frac{1}{2}\frac{\partial B_z}{\partial y} + \frac{\partial B_1^{\pm}}{\partial z} \end{bmatrix} \end{aligned} \tag{2.18}$$

First, magnitude and phase parts of each of these terms in Equation 2.18 is written seperately. Then, assuming $\nabla|B_1^+| = 0$ and $\nabla|B_1^-| = 0$, removal of common term ($|B_1^{\pm}|e^{i\phi^{\pm}}$) Equation 2.18 becomes:

$$\Omega^{\pm} \cdot \nabla \ln(\gamma) + \left(\left(\left(\frac{\partial \phi^{\pm}}{\partial x} \right)^2 + \left(\frac{\partial \phi^{\pm}}{\partial y} \right)^2 + \left(\frac{\partial \phi^{\pm}}{\partial z} \right)^2 \right) - i\nabla^2 \phi^{\pm} \right) + i\omega\mu_0\gamma = 0 \tag{2.19}$$

where

$$\Omega^{\pm} = \begin{bmatrix} i\frac{\partial}{\partial x}\phi^{\pm} \pm \frac{\partial}{\partial y}\phi^{\pm} \\ \mp\frac{\partial}{\partial x}\phi^{\pm} + i\frac{\partial}{\partial y}\phi^{\pm} \\ i\frac{\partial}{\partial z}\phi^{\pm} \end{bmatrix} + \frac{1}{B_1^{\pm}} \begin{bmatrix} \frac{1}{2}\frac{\partial B_z}{\partial z} \\ \pm i\frac{1}{2}\frac{\partial B_z}{\partial z} \\ -\frac{1}{2}\frac{\partial B_z}{\partial x} \mp i\frac{1}{2}\frac{\partial B_z}{\partial y} \end{bmatrix} \tag{2.20}$$

However, there are some problems related to Equation 2.19. First, B_z cannot be measured via MRI. To get rid of this, one can say that derivatives of B_z is negligible, therefore second term of $\Omega^{\pm}$ will vanish. Second, the transmit or receive phases cannot be measured using MRI directly. To solve this issue, both transmit and receive versions of Equation 2.19 is summed. Then, equation 2.19 becomes:

$$\begin{bmatrix} i\frac{\partial}{\partial x}\phi^{tr} + \frac{\partial}{\partial y}(\phi^{+} - \phi^{-}) \\ \frac{\partial}{\partial x}(-\phi^{+} + \phi^{-}) + i\frac{\partial}{\partial y}\phi^{tr} \\ i\frac{\partial}{\partial z}\phi^{tr} \end{bmatrix} \cdot \begin{bmatrix} \frac{\partial \ln(\gamma)}{\partial x} \\ \frac{\partial \ln(\gamma)}{\partial y} \\ \frac{\partial \ln(\gamma)}{\partial z} \end{bmatrix} + (k_{real} - i\nabla^2\phi^{tr}) + i2\omega\mu_0\gamma = 0 \tag{2.21}$$

where

$$\begin{aligned} k_{real} = &\left(\frac{\partial}{\partial x}\phi^{tr}\right)^2 + \left(\frac{\partial}{\partial y}\phi^{tr}\right)^2 + \left(\frac{\partial}{\partial z}\phi^{tr}\right)^2 \\ &- 2\left(\frac{\partial}{\partial x}\phi^{-}\frac{\partial}{\partial x}\phi^{+} + \frac{\partial}{\partial y}\phi^{-}\frac{\partial}{\partial y}\phi^{+} + \frac{\partial}{\partial z}\phi^{-}\frac{\partial}{\partial z}\phi^{+}\right) \end{aligned} \tag{2.22}$$

Similar to standard phase based approach, one should focus on the imaginary part of this equation to find conductivity. Imaginary part of 2.19 is:

$$\begin{aligned} &\begin{bmatrix} \frac{\partial}{\partial x}\phi^{tr} \\ \frac{\partial}{\partial y}\phi^{tr} \\ \frac{\partial}{\partial z}\phi^{tr} \end{bmatrix} \cdot \begin{bmatrix} \frac{\partial \mathrm{Re}(\ln(\gamma))}{\partial x} \\ \frac{\partial \mathrm{Re}(\ln(\gamma))}{\partial y} \\ \frac{\partial \mathrm{Re}(\ln(\gamma))}{\partial z} \end{bmatrix} + \begin{bmatrix} \frac{\partial}{\partial y}(\phi^{+} - \phi^{-}) \\ -\frac{\partial}{\partial x}(\phi^{+} - \phi^{-}) \\ 0 \end{bmatrix} \cdot \begin{bmatrix} \frac{\partial \mathrm{Im}(\ln(\gamma))}{\partial x} \\ \frac{\partial \mathrm{Im}(\ln(\gamma))}{\partial y} \\ \frac{\partial \mathrm{Im}(\ln(\gamma))}{\partial z} + \end{bmatrix} \\ &- \nabla^2\phi^{tr} + 2\omega\mu_0\sigma = 0 \end{aligned} \tag{2.23}$$

It is shown in simulations that derivatives of $\phi^{+} - \phi^{-}$ is much smaller than derivatives of $\phi^{+} + \phi^{-}$ [24]. Therefore, second term can be neglected. In addition to this, for $\sigma^2 \gg (\omega\varepsilon)^2$, $\mathrm{Re}(\ln(\gamma)) = \ln(\sqrt{\sigma^2 + (\omega\varepsilon)^2})$ can be approximated as $\ln(\sigma)$. By using $\nabla \ln(\sigma) = -\frac{1}{\rho}\nabla\rho$, Equation 2.23 becomes:

$$(\nabla\phi^{tr} \cdot \nabla\rho) + \nabla^2\phi^{tr}\rho - 2\omega\mu_0 = 0 \tag{2.24}$$

where $\rho = 1/\sigma$.

Chapter 3

bSSFP Phase Correction and its use in MREPT

To reconstruct conductivity maps, any MRI sequence that provides B_1^+ phase can be utilized. Commonly used sequences are spin-echo [33], gradient-echo [34], ultra-short echo (UTE) / zero echo time (ZTE) [35, 36] and bSSFP [25]. Spin-echo based sequences suffer from eddy current effects and lengthy acquisition time. Gradient-echo based sequences suffer from off-resonance effect, which needs to be corrected by additional B_0 mapping. In addition to this, eddy current effects and acquisition time are still problematic. Despite being fast sequences, UTE/ZTE suffer from streaking artifacts which deteriorate the phase images and such artifacts can be amplified through Laplacian operation and distort the final conductivity image. bSSFP is widely used in MREPT field, because of its speed, SNR, motion insensitivity and automatic eddy current compensation [19, 25]. However, in certain off-resonance frequencies, "banding artifact" occurs. Banding artifact manifests itself as magnitude drop and phase jump with an amount of π.

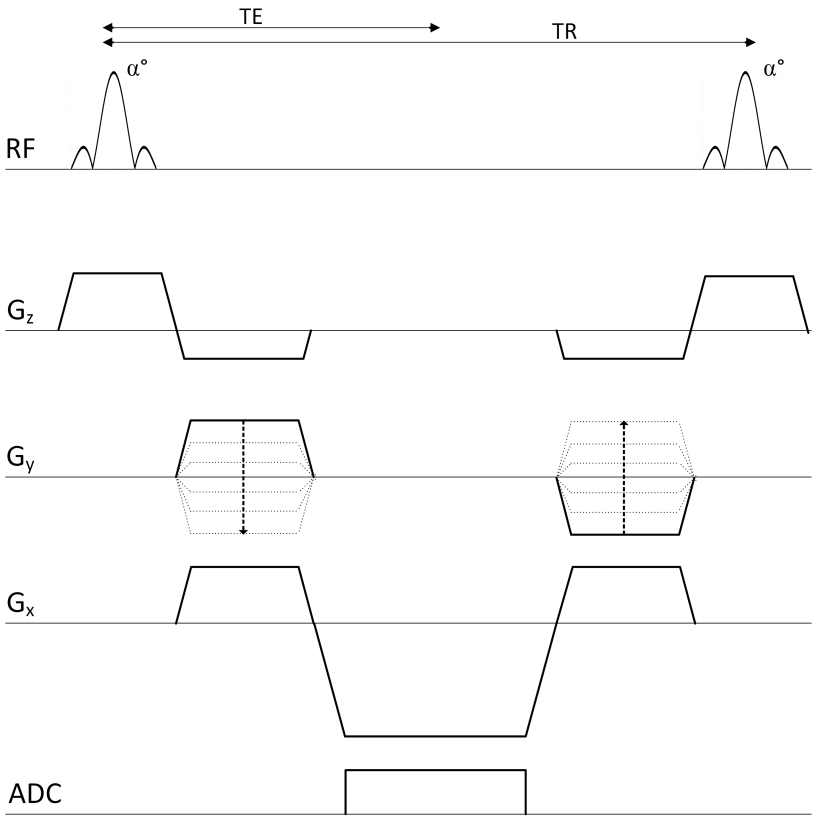

Figure 3.1: Pulse sequence diagram balanced steady state free precession (bSSFP) sequence.

3.1 Theory of bSSFP - Complex Image Values at Steady State

bSSFP pulse sequence diagram is shown in Figure 3.1. To investigate the effect of the banding artifact thoroughly, one should focus on the complex image values at the steady state. The steady state magnetization vector ($\mathbf{M}$) right after the $-\alpha$ flip angle along the x-axis can be written as:

$$\begin{aligned}\mathbf{M}(n\mathrm{TR}^{+}) &= \begin{bmatrix} 1 & 0 & 0 \\ 0 & \cos\alpha & \sin\alpha \\ 0 & -\sin\alpha & \cos\alpha \end{bmatrix} \mathbf{M}(n\mathrm{TR}^{-}) \\ &= \mathbf{R}_x(-\alpha)\mathbf{M}(n\mathrm{TR}^{-})\end{aligned} \tag{3.1}$$

In each TR, magnetization vector is affected by off-resonance, RF phase increment (in phase-cycling bSSFP sequences), precession along xy-plane and relaxation along z-axis. Therefore, we get:

$$\begin{aligned}\mathbf{M}((n+1)\mathrm{TR}^-) =& \mathbf{R}_z((\Omega+\Delta\Omega)\mathrm{TR})\mathbf{D}(\mathrm{TR}) \\ & \times \mathbf{M}(n\mathrm{TR}^+) + (1-E_1)\mathbf{M}_0\end{aligned} \tag{3.2}$$

where

$$D(t) = \begin{bmatrix} e^{-t/\mathrm{T}_2} & 0 & 0 \\ 0 & e^{-t/\mathrm{T}_2} & 0 \\ 0 & 0 & e^{-t/\mathrm{T}_1} \end{bmatrix}$$

$$E_1 = e^{-\mathrm{TR}/\mathrm{T}_1}$$

$$\mathbf{M}_0 = [0, 0, \mathrm{M}_0]^T$$

$$\Omega = 2\pi\Delta\mathrm{f}_0$$

$\Delta\mathrm{f}_0$ is off-resonance frequency and $\Delta\Omega\mathrm{TR}$ is user-controlled RF phase increment in each TR.

Since at steady state, $\mathbf{M}(n\mathrm{TR}^-) = \mathbf{M}((n+1)\mathrm{TR}^-)$ and $\mathbf{M}(n\mathrm{TR}^+) = \mathbf{M}((n+1)\mathrm{TR}^+)$, using Equations 3.1 and 3.2 together:

$$\begin{aligned}\mathbf{M}(\mathrm{TR}^+) = & (\mathbf{I} - \mathbf{R}_x(\alpha)\mathbf{R}_z((\Omega+\Delta\Omega)\mathrm{TR})\mathbf{D}(\mathrm{TR}))^{-1} \\ & \times (1-E_1)\mathbf{R}_x(-\alpha)\mathbf{M}_0\end{aligned} \tag{3.3}$$

Using Equation 3.3, magnetization vector at TE can be found as follows:

$$\begin{aligned}\mathbf{M}(\mathrm{TE}) =& \mathbf{R}_z(\Omega\mathrm{TE})\mathbf{D}(\mathrm{TE})\mathbf{M}(\mathrm{TR}^+) \\ & + (1-E_1)\mathbf{M}_0\end{aligned} \tag{3.4}$$

Defining $M = M_x(\mathrm{TE}) + iM_y(\mathrm{TE})$ and including coil sensitivity, K, whose phase is the transceive phase of the RF system, complex image value at an arbitrary pixel in the slice of interest, S_n, can be expressed as:

$$S_n = KM = KM_1 e^{-\mathrm{TE}/\mathrm{T}_2} e^{i\Omega TE} \frac{1 - ae^{-i(\Omega+\Delta\Omega_n)\mathrm{TR}}}{1 - b\cos((\Omega+\Delta\Omega_n)\mathrm{TR})} \tag{3.5}$$

where

$$M_1 = iM_0 \frac{(1-E_1)\sin\alpha}{1-E_1\cos\alpha-(E_1-\cos\alpha)E_2^2}$$
$$a = E_2$$
$$b = \frac{E_2(1-E_1)(1+\cos\alpha)}{1-E_1\cos\alpha-(E_1-\cos\alpha)E_2^2}$$
$$E_2 = e^{-\mathrm{TR}/\mathrm{T}_2}$$

Figure 3.2 demonstrates magnitude and phase of M with respect to off-resonance frequency as obtained from Equation 3.5. Figures 3.2a and 3.2b are for a large T_2 (1000 ms). Concentrating on the magnitude graph (Fig. 3.2a), we observe that for $\pm\frac{1}{2\mathrm{TR}}$, the magnitude of M is maximum. However, as the off-resonance frequency changes, magnitude begins to decrease and in fact the decrease becomes substantial as this off-resonance frequency change approaches to $\frac{1}{2\mathrm{TR}}$ (banding artifact). This off-resonance behaviour is periodic with a period of $\frac{1}{\mathrm{TR}}$. As also found in the literature, the off-resonance frequency range is divided into two parts, called the "pass-band" and the "stop-band" regions [37]. The pass-band region corresponds to a region in which magnitude is high, and the stop-band region corresponds to the region where magnitude is low. These two regions are non-intersecting and their union covers the whole range. The exact definition of these regions depend on the application and the purpose of the study [37]. In our case, we have decided to determine them as follows: In base period $[-\frac{1}{2\mathrm{TR}} < f < \frac{1}{2\mathrm{TR}}]$, stop-band region is defined as $[-\frac{1}{4\mathrm{TR}} < f < \frac{1}{4\mathrm{TR}}]$, and the pass-band region is the rest of the period. The boundaries of these regions are shown in Figure 3.2 for the base period and also for the adjacent periods.

When we look at the phase graphs, we observe that in the pass-band regions, phases are almost constant; however in the middle of stop-band regions a jump of π radians is observed. This jump in fact corresponds to the phase jump in the banding artifact of bSSFP images. Please note that these observations are made for the case of large T_2 (namely T_2 = 1000 ms). Figures 3.2c and 3.2d present the graphs for a small T_2 (40 ms). One can observe that the magnitude plot does not display a constant plateau behaviour even in the pass-band region. Similarly, the phase graph also does not display almost constant behaviour in the

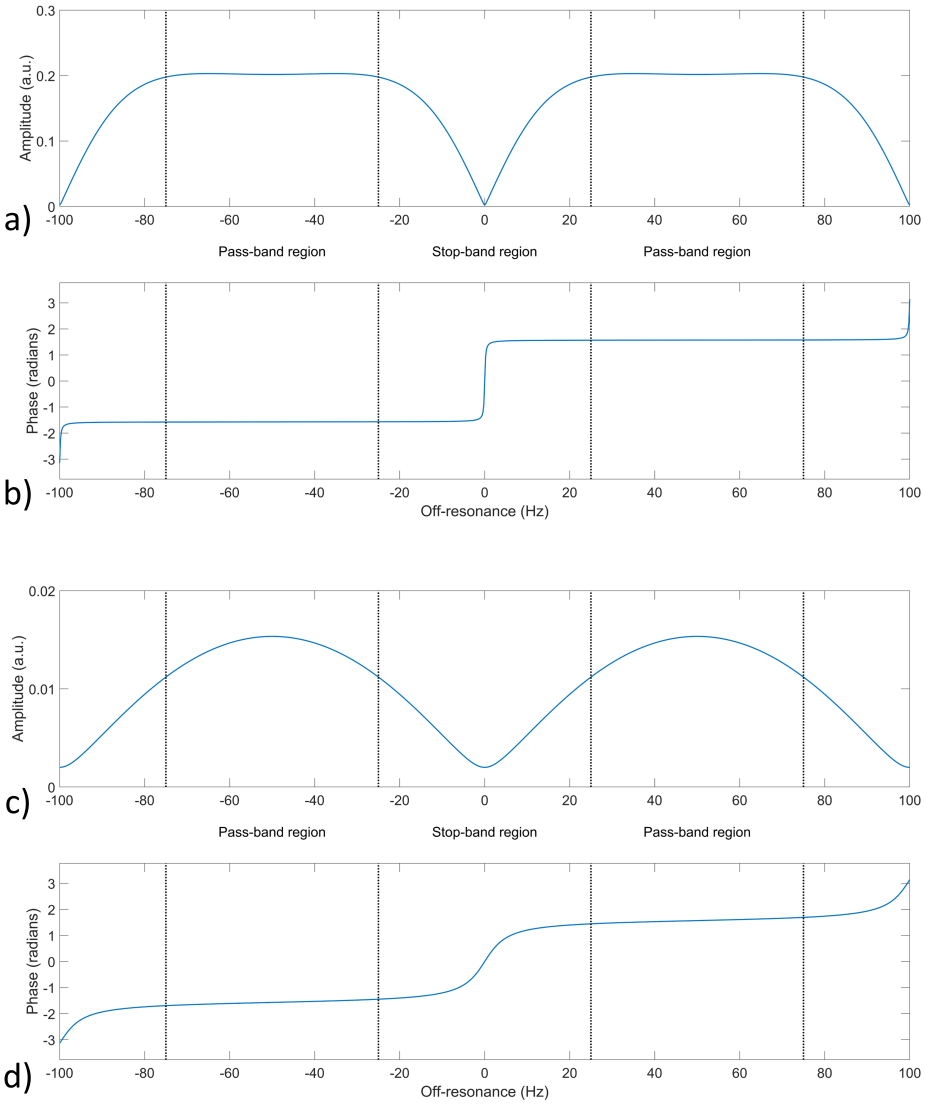

Figure 3.2: **(a)** Magnitude and **(b)** phase of the steady state magnetization as a function of off-resonance for $T_2 = 1000$ ms, and **(c,d)** $T_2 = 40$ ms are shown. Simulation parameters are: $T_1 = 6000$ ms, TE $= 5$ ms, TR $= 10$ ms, flip angle $= 40°$.

pass-band regions, but displays a variation dependent on both ΔB_0 and T_2. For example, in the pass-band region, dependence on ΔB_0 is almost linear and the slope is equal to $\frac{1}{2} - \frac{E_2}{1+E_2}$. We called this variation of phase in the pass-band regions as "non-constant plateau effect".

3.2 Methods

3.2.1 Correction Methods of bSSFP Phase

3.2.1.1 Inserting B_0 and T_2 Information

In bSSFP imaging, the complex image value at an arbitrary pixel in the slice of interest using alternating RF pulses can be expressed as:

$$S = KM = KM_1 e^{-\mathrm{TE}/\mathrm{T_2}} e^{i(\mathrm{f_{OR}}+\Delta \mathrm{f_s})\mathrm{TE}} \frac{1 + ae^{-i2\pi(\mathrm{f_{OR}}+\Delta \mathrm{f_s})\mathrm{TR}}}{1 + b\cos(2\pi(\mathrm{f_{OR}} + \Delta \mathrm{f_s})\mathrm{TR})} \tag{3.6}$$

where

$$\begin{aligned} M_1 &= iM_0 \frac{(1 - E_1)\sin\alpha}{1 - E_1\cos\alpha - (E_1 - \cos\alpha)E_2^2} \\ a &= E_2 \\ b &= \frac{E_2(1 - E_1)(1 + \cos\alpha)}{1 - E_1\cos\alpha - (E_1 - \cos\alpha)E_2^2} \\ E_2 &= e^{-TR/T_2} \end{aligned}$$

T_1 and T_2 represent longitudinal and transversal relaxation times, TE and TR are echo time and repetition time, α is flip angle, M_0 is equilibrium magnetization, f_{OR} is off-resonance frequency due to ΔB_0, Δf_s is the frequency shift in the excitation frequency as controlled by the user, and lastly K is the complex valued factor the phase of which is the transceive phase of the RF system (sum of transmit phase and receive phase). Although magnitude of S is dependent on many parameters, phase of it, which is the measured bSSFP phase, is relatively simple and can be expressed as:

$$\angle(S) = \angle(K) + \angle(M) \tag{3.7}$$

where

$$\angle(M) = 2\pi(\mathrm{f_{OR}} + \Delta\mathrm{f_s})\mathrm{TE} + \angle(1 + \mathrm{E_2}e^{-i2\pi(\mathrm{f_{OR}}+\Delta\mathrm{f_s})\mathrm{TR}}) \tag{3.8}$$

In Equation 3.7, $\angle(K)$ is what we are interested in and $\angle(M)$ can be viewed as a phase error term. In the expression for the phase error term, the independent variables are $\mathrm{T_2}$ (through $\mathrm{E_2}$), the off-resonance frequency $\mathrm{f_{OR}}$, TE, TR, and the excitation frequency shift $\Delta\mathrm{f_s}$. Among these, TE, TR and the excitation frequency shift are determined by the user. Therefore, by making use of methods for determining the off-resonance frequency and $\mathrm{T_2}$ values for each pixel, we can obtain the correct value of transceive phase for each pixel using Equations 3.7 and 3.8. Figure 3.3 demonstrates magnitude and phase of M with respect to off-resonance frequency as obtained from Equation 3.6. Figures 3.3a and 3.3b are for a large $\mathrm{T_2}$ (1000 ms). Also in these parts, the graphs are given for two cases: (1) Frequency shift $\Delta\mathrm{f_s}$ equals zero (blue lines), (2) Frequency shift $\Delta\mathrm{f_s}$ equals 1/2TR (red lines). In this case, pass-band and stop-band regions are defined as follows: In the base period $[-\frac{1}{2\mathrm{TR}} < f < \frac{1}{2\mathrm{TR}}]$, pass-band region is defined as $[-\frac{1}{4\mathrm{TR}} < f < \frac{1}{4\mathrm{TR}}]$, and the stop-band region is the rest of the period. For the graph for which excitation frequency shift is equal to $(2\mathrm{TR})^{-1}$ (red lines in Figures 3.3a and 3.3b), we observe that the magnitude and phase graphs shift exactly by an amount of $(2\mathrm{TR})^{-1}$ with respect to the blue lines. Therefore, using the same definition of pass-band and stop-band regions for these red graphs reveal regions such that the pass-band region of the blue graphs corresponds exactly to the stop-band regions for these red graphs and vice versa.

The method comprises the acquisition of two bSSFP images, one $\mathrm{B_0}$ map, and one $\mathrm{T_2}$ map. Using the information contained in the $\mathrm{B_0}$ map, a bSSFP image is segmented into two segments (set of pixels). One segment corresponds to pixels for which $\Delta\mathrm{B_0}$ lies in the pass-band region of the magnetization vs off-resonance curves shown in Figure 3.3, and the other segment contains pixels at which $\Delta\mathrm{B_0}$ corresponds to the stop-band region. The two bSSFP images are obtained with different excitation frequencies. Difference between the two excitation frequencies is selected as $(2\mathrm{TR})^{-1}$, since the periodicity of the regions (pass-band and stop-band) is $(\mathrm{TR})^{-1}$ (How these excitation frequencies are determined is explained in Sequence Parameters section). In this way, we have complementary images such

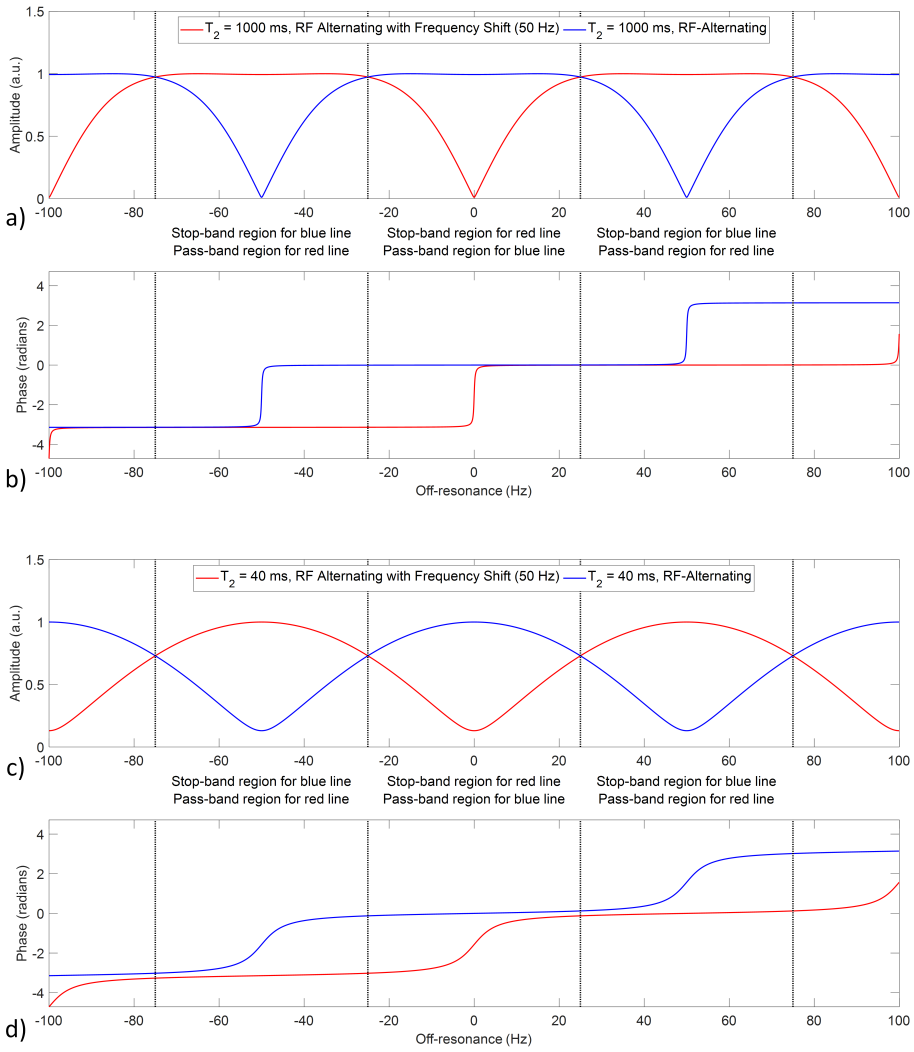

Figure 3.3: **(a)** Magnitude and **(b)** phase of the steady state magnetization as a function of off-resonance for $T_2 = 1000$ ms, and **(c,d)** $T_2 = 40$ ms are shown. Blue lines correspond to the magnetizations which are obtained with bSSFP sequence using alternating RF pulse, while red lines correspond to the same sequence but excitation frequency difference of 50 Hz. Simulation parameters are: $T_1 = 6000$ ms, TE = 5 ms, TR = 10 ms, flip angle = 40°.

that, if one pixel lies in the pass-band segment in one bSSFP image, it lies in the stop-band segments in the other bSSFP image. The boundaries between the pass-band and stop-band segments are called "the band transition boundaries". A third image is generated by combining the pass-band segments extracted from each of the bSSFP images. In other words, this "collaged" image is formed by making use of the banding artifact free segments of each of the two bSSFP images. However, the phase of the collaged image still has contributions from the phase error term explained in Equations 3.7 and 3.8. Phase error is calculated for any pixel by $\angle(M)$ as given in Equation 3.8, using the T_2 and ΔB_0 values of that pixel. Calculated phase error is subtracted from the collaged image to obtain T_2 and ΔB_0 corrected phase images. If T_2 map is not available, one can take $E_2 = 1$ and make the phase correction accordingly, in which case the corrected phase image is called "Type-I corrected phase image". If both T_2 and ΔB_0 maps are available, E_2 is assigned to its correct value for each pixel and the corrected phase image is called "Type-II corrected phase image".

3.2.1.2 Linearization for Off-Resonance Estimation - Gauss-Newton Nonlinear Search (LORE-GN) Algorithm

Linearization for off-resonance estimation - Gauss-Newton nonlinear search (LORE-GN) algorithm is first suggested by Björk [28]. With the introduction of independent and complex Gaussian distributed noise, v_n, Equation 3.5 becomes:

$$S_n = KM = KM_1 e^{-\mathrm{TE}/\mathrm{T}_2} e^{i\Omega TE} \frac{1 - ae^{-i(\Omega+\Delta\Omega_n)\mathrm{TR}}}{1 - b\cos((\Omega + \Delta\Omega_n)\mathrm{TR})} + v_n \tag{3.9}$$

By introducing following variables:

$$\begin{aligned} S_0 &= KM_1 e^{-\mathrm{TE}/\mathrm{T}_2}, \\ \theta &= \Omega\mathrm{TR}, \\ \Delta\theta_n &= \Delta\Omega_n\mathrm{TR}, \\ \theta_n &= \theta + \Delta\theta_n. \end{aligned} \tag{3.10}$$

pixel-wise signal model becomes:

$$S_n = S_0 e^{i\theta\mathrm{TE}/\mathrm{TR}} \frac{1 - ae^{-i\theta_n}}{1 - b\cos(\theta_n)} + v_n = g_n(\mathbf{u}) + v_n \tag{3.11}$$

where $g_n(\mathbf{u})$ is pure data model of nth phase-cycle image. Unknowns from Equation 3.11 form $\mathbf{u}$ vector, which equals to $\mathbf{u} = [\theta, \mathrm{Re}(S_0), \mathrm{Im}(S_0), a, b]^T$. With the introduction of following parameters:

$$\begin{aligned}\eta &= S_0 e^{i\theta TE/TR},\\ \beta &= S_0 a e^{i\theta(TE/TR-1)},\\ \zeta &= b e^{i\theta}.\end{aligned}$$

Equation 3.11 becomes:

$$S_n = \frac{\eta - \beta e^{-i\Delta\theta_n}}{1 - \mathrm{Re}(\zeta e^{i\Delta\theta_n})} \tag{3.12}$$

From now on, for the sake of simplicity, subscripts r and i stand for real and imaginary parts respectively. If we do cross multiplication:

$$S_n[1 - \zeta_r cos(\Delta\theta_n) + \zeta_i sin(\Delta\theta_n)] = \eta - \beta e^{-i\Delta\theta_n} \tag{3.13}$$

With the definition of $\mathbf{y}_n = [S_{r,n} S_{i,n}]^T$, Equation 3.13 becomes:

$$\mathbf{y}_n = \underbrace{\begin{bmatrix} 1 & 0 & -\cos(\Delta\theta_n) & -\sin(\Delta\theta_n) & S_{r,n}\cos(\Delta\theta_n) & -S_{r,n}\sin(\Delta\theta_n) \\ 0 & 1 & \sin(\Delta\theta_n) & -\cos(\Delta\theta_n) & S_{i,n}\cos(\Delta\theta_n) & -S_{i,n}\sin(\Delta\theta_n) \end{bmatrix}}_{\mathbf{A}_n} \underbrace{\begin{bmatrix} \eta_r \\ \eta_i \\ \beta_r \\ \beta_i \\ \zeta_r \\ \zeta_i \end{bmatrix}}_{\mathbf{x}} \tag{3.14}$$

Concatenating the measurements, $\mathbf{y}$ and $\mathbf{A}$ matrices are constructed as follows:

$$\begin{aligned}\mathbf{y} &= [\mathbf{y}_1 \cdots \mathbf{y}_N]^T\\ \mathbf{A} &= [\mathbf{A}_1^T \cdots \mathbf{A}_N^T]^T\end{aligned} \tag{3.15}$$

After that, to obtain unknown vector, $\mathbf{x}$, from $\mathbf{y} = \mathbf{A}\mathbf{x}$, least squares estimation is used as follows:

$$\hat{\mathbf{x}} = (\mathbf{A}^T\mathbf{A})^{-1}\mathbf{A}^T\mathbf{y} \tag{3.16}$$

Then, using $\mathbf{x}$ vector, parameters from Equations 3.9 and 3.10 can be estimated as:

$$\begin{aligned}\hat{\theta} &= -\angle(\hat{\beta}/\hat{\eta}),\\ \hat{a} &= |\hat{\beta}/\hat{\eta}|,\\ \hat{b} &= |\hat{\zeta}|\\ \hat{S}_0 &= \hat{\eta}e^{-i\hat{\theta}\mathrm{TE/TR}}\end{aligned}$$

Although this formulation alone gives accurate estimation of the unknowns, it is not the optimal solution in NLS sense. Therefore, after having initial estimation, Gauss-Newton iterative method is used to obtain global optimum with high probability. The NLS criterion is

$$L(\mathbf{u}) = \sum_{n=1}^{N} |S_n - g_n(\mathbf{u})|^2 \tag{3.17}$$

Defining $\mathbf{r}$ as:

$$r = \begin{bmatrix}\mathrm{Re}(\mathbf{S})\\ \mathrm{Im}(\mathbf{S})\end{bmatrix} - \begin{bmatrix}\mathrm{Re}(\mathbf{g}(\mathbf{u}))\\ \mathrm{Im}(\mathbf{g}(\mathbf{u}))\end{bmatrix} \tag{3.18}$$

the update formula with the direction of change, $\mathbf{p}_k$ is:

$$\mathbf{u}_{k+1} = \mathbf{u}_k + c\mathbf{p}_k = \mathbf{u}_k + c(\mathbf{J}_k^T\mathbf{J}_k)^{-1}\mathbf{J}_k^T\mathbf{r}_k \tag{3.19}$$

where $\mathbf{J}_k = \mathbf{J}(\mathbf{u})|_{\mathbf{u}=\mathbf{u}_k}$ is Jacobian matrix at the point $\mathbf{u}_k$ and initial $\mathbf{u}$ is taken as $\mathbf{u}_0 = [\theta, \mathrm{Re}(KM_0), \mathrm{Im}(KM_0), T_1, T_2]$ The step length, c, is chosen as 2^{-m}, where m is smallest non-negative integer that satisfies:

$$L(\mathbf{u}_{k+1}) \leq L(\mathbf{u}_k) - \mu c\mathbf{r}_k^T\mathbf{J}_k(\mathbf{J}_k^T\mathbf{J}_k)^{-1}\mathbf{J}_k^T\mathbf{r}_k \tag{3.20}$$

In this equation, μ is selected as 0.5 and stopping criterion is $||\mathbf{J}_k^T\mathbf{r}_k|| < 10^{-8}$. After founding optimal $\mathbf{u}$, estimated RF transceive phase can easily be obtained via:

$$\angle(K) = \tan^{-1}\left(\frac{\mathrm{Im}(KM_0)}{\mathrm{Re}(KM_0)}\right) \tag{3.21}$$

3.2.1.3 PLANET Method

There is no known full form for PLANET. Yet we can speculate that the name "PLANET" is chosen due to the elliptical nature of this method which will be

explained later. PLANET method is first suggested by Shcherbakova [29]. Similar to Equation 3.5, complex signal S_n can be expressed as:

$$S_n = M_{\text{eff}} \cdot \frac{1 - ae^{-i\theta_n}}{1 - b\cos\theta_n} \cdot e^{i\varphi} \tag{3.22}$$

where

$$\begin{aligned} \varphi_{rot} &= 2\pi(\delta_{CS} + \Delta f_0)\text{TE} + \varphi_{RF} + \varphi_{eddy} \\ M_{eff} &= K' M e^{-\text{TE}/\text{T}_2} \\ \theta_n &= \theta_0 + \Delta\theta_n \end{aligned} \tag{3.23}$$

K′ is the magnitude of the combined field (receive and transmit), φ_{RF} is the RF transceive phase and φ_{eddy} is phase error due to eddy current effects.

By concatenating the same pixel for each phase-cycled bSSFP image (S_n), a set of pixels is obtained. Then, this set is fitted to an ellipse in a linear least squares sense. Fitted ellipse can be described as:

$$F(x) = C_1x^2 + C_2xy + C_3y^2 + C_4x + C_5y + C_6 \tag{3.24}$$

where x and y are real and imaginary parts of the set of pixels, respectively. By using the known values of x and y, $\mathbf{C} = [C_1, C_2, C_3, C_4, C_5, C_6]$ can be found. After that, φ_{rot} can be obtained as (see Figure 3.4):

$$\varphi_{rot} = \frac{1}{2} \cdot \tan^{-1}\left(\frac{C_2}{C_1 - C_3}\right) \tag{3.25}$$

By finding φ_{rot}, rotation is removed and the center of the ellipse becomes located on the x-axis. Then, conic equation can be written as:

$$\frac{(x - x_c)^2}{A^2} + \frac{y^2}{B^2} = 1 \tag{3.26}$$

where (x_c, 0) is the center of the ellipse, A and B are the semi-axes of the ellipse. Parameters of Equation 3.26 (x_c, A, B) and parameters of Equation 3.22 (a, b, M_{eff}) are connedted by the following set of equations:

$$\begin{aligned} x_C &= M_{eff}\frac{1 - ab}{1 - b^2} \\ A &= M_{eff}\frac{|a - b|}{1 - b^2} \\ B &= M_{eff}\frac{a}{\sqrt{1 - b^2}} \end{aligned} \tag{3.27}$$

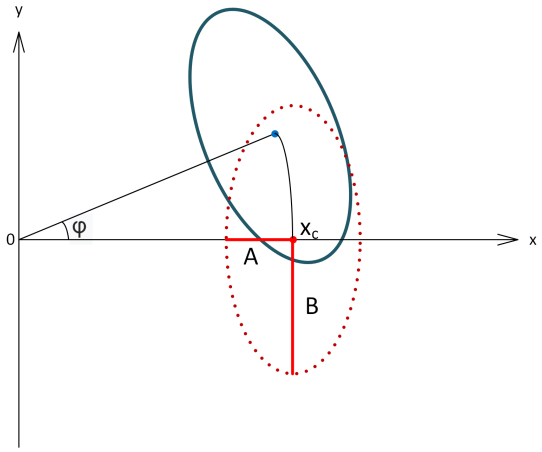

Figure 3.4: Ellipse formations before φ_{rot} is removed (solid blue line) and after (dotted red line) are shown.

By choosing $a > b$, or in other words $\alpha > cos^{-1}(E_1)$, we can obtain a, b and M_{eff} as follows:

$$\begin{aligned} b &= \frac{-x_c A + \sqrt{(x_c A)^2 - (x_c^2 + B^2)(A^2 - B^2)}}{x_c^2 + B^2} \\ a &= \frac{B}{x_c\sqrt{1-b^2} + bB} \\ M_{eff} &= \frac{x_c(1-b^2)}{1-ab} \end{aligned} \tag{3.28}$$

To obtain RF transceive phase, first we need to find Δf_0. In Equation 3.22, θ_n can be expressed as:

$$\theta_n = \theta_0 + \Delta\theta_n = 2\pi \mathrm{TR}\Delta f_0 + \Delta\theta_n \tag{3.29}$$

From ellipse formulation:

$$\begin{aligned} x &= x_c + A\mathrm{cos}t \\ y &= B\mathrm{sin}t \end{aligned} \tag{3.30}$$

where

$$t = \tan^{-1}\left(\frac{A}{B}\tan\beta\right)$$

Using Equations 3.22 and 3.30 together for each data point with n=0,1,...,N-1:

$$cos\theta_n = \frac{\cos t_n - b}{b\cos t_n - 1} \tag{3.31}$$

By using $\cos\theta_n = \cos(\theta_0 + \Delta\theta_n) = \cos\theta_0 \cos\Delta\theta_n - \sin\theta_0 \sin\Delta\theta_n = K_1 \cos\Delta\theta_n + K_2 \sin\Delta\theta_n$, θ_0 can be found in a least squares sense:

$$\theta_0 = \tan^{-1} \frac{K_2}{K_1} \tag{3.32}$$

Combining Equation 3.23 and 3.29, one can find φ_{RF}, which is RF transceive phase.

3.2.2 Experimental Methods

3.2.2.1 Sequence Parameters

Experiments were conducted on 3T Siemens Tim Trio MR scanner using a quadrature body coil for both transmit and receive purposes.

For LORE-GN algorithm and PLANET method, 16 phase-cycled bSSFP images are obtained with the RF phase increment of $\pi - \frac{n \cdot 2\pi}{16}$ where $n = 0, 1, ..., 15$. The scan parameters were: TE/TR = 2.29/4.58 ms, matrix size = 128x128x60, flip angle (FA) = 40°, field of view (FoV) = 225 mm, slice thickness = 2 mm, number of averages (NEX) = 1, duration for each scan = 35 seconds.

For first method (inserting B_0 and T_2 directly), two bSSFP images are obtained. For first phantom experiment, scan parameters were: TE/TR = 4.98/9.96 ms, matrix size = 128x128x20, FA = 40°, FoV = 225 mm, slice thickness = 1.5 mm, NEX = 32, duration for each scan = 5 minutes 29 seconds. For second phantom experiment, scan parameters were: TE/TR = 4.98/9.96 ms, matrix size = 128x128x60, FA = 40°, FoV = 225 mm, slice thickness = 2 mm, NEX = 1, duration for each scan = 76 seconds. For human experiment, scan parameters were: TE/TR = 5/10 ms, matrix size = 128x128x60, FA = 40°, FoV = 225 mm, slice thickness = 1.5 mm, NEX = 8, duration for each scan = 10 minutes and 18 seconds. For the first bSSFP sequence, the excitation frequency, f_1 is determined by the MRI system itself. For the second bSSFP sequence, we have used an RF frequency, f_2, which is equal to $f_1 + 50$ Hz. Since TR is equal to 10 ms, the frequency shift is chosen as $(2\text{TR})^{-1} = 50$ Hz.

B_0 is obtained by using the double echo method which involves two gradient echo images with different TEs [38]. The sequence parameters in the first phantom experiment were: TE = 10 or 15 ms, TR = 3500 ms, matrix size = 128x128x20, FA = 60°, FoV = 225 mm, slice thickness = 1.5 mm, NEX = 1, duration for each scan = 7 minutes 33 seconds. The sequence parameters in the second phantom experiment were: TE = 10 or 15 ms, TR = 3500 ms, matrix size = 128x128x60, FA = 60°, FoV = 225 mm, slice thickness = 2 mm, NEX = 1, duration for each scan = 7 minutes 33 seconds. For human experiment, scan parameters were: TE = 10 or 15 ms, TR = 3500 ms, matrix size = 128x128x60, FA = 60°, FoV = 225 mm, slice thinkness = 1.5 mm, NEX = 8, duration for each scan is 7 minutes 33 seconds. T_2 map is obtained via series of single echo spin-echo sequences with different TEs by using the exponential T_2 fitting method whose result is accepted as the ground truth for many investigators [39,40]. For first phantom experiment, scan parameters were: TE = 13, 30, 50, 75, 100, or 150 ms, TR = 6500 ms, matrix size = 128x128x20, FoV = 225 mm, slice thickness = 1.5 mm, NEX = 1 mm, duration for each scan = 14 minutes. For second phantom experiment, scan parameters were: TE = 13, 30, 50, 75, or 100 ms, TR = 6500 ms, matrix size = 128x128x60, FoV = 225 mm, slice thickness = 2 mm, NEX = 1 mm, duration for each scan = 14 minutes. For human experiment, scan parameters were: TE = 13, 40, 75 or 100 ms, TR = 6500 ms, matrix size = 128x128x60, FoV = 225 mm, slice thickness = 1.5 mm, NEX = 1, duration for each scan = 14 minutes. Note that, the gradient echo and the spin echo sequences that we have mentioned above are all multi-slice sequences in which data are collected from all slices within one TR, and therefore the total duration of such multi-slice scans is dependent on TR and not dependent on the number of slices. Both of the B_0 and T_2 maps are obtained by using the RF excitation frequency equal to f_1.

3.2.2.2 Phantom Parameters

For first method, a cylindrical, z-independent experimental phantom with diameter of 20 cm and height of 25 cm was constructed. For background region, agar-salive gel (20 g/L agar, 2 g/L NaCl, 0.2 g/L $CuSO_4$ was used), and for

anomalies, longitudinal holes were drilled and filled with saline solution (6 g/L NaCL, 0.2 g/L $CuSO_4$). The conductivity values for background and the anomaly regions are expected to be 0.5 and 1 S/m respectively [20]. Anomaly regions have diameters of 0.5, 1.5 and 2.5 cm.

For all methods, another cylindrical, z-independent experimental phantom with diameter of 20 cm and height of 25 cm was constructed. For background region, agar-salive gel (20 g/L agar, 2 g/L NaCl, 1.5 g/L $CuSO_4$ was used), and for anomalies, longitudinal holes were drilled and willed with saline solution (6 g/L NaCL, 1.5 g/L $CuSO_4$).

3.2.2.3 In Vivo Human Experiment

MRI scans were performed on a healthy male volunteer of age 25 after obtaining written informed consent in line with the approval of the Institutional Review Board of Bilkent University.

3.3 Results

3.3.1 Inserting B_0 and T_2 Information

For first phantom experiment, magnitude and phase of the phantom images obtained by the two bSSFP sequences are shown in Figure 3.5. Figures 3.5a and 3.5c correspond to the RF alternating bSSFP sequence applied by using the RF frequency which is determined by the MRI system, f_1. Figures 3.5b and 3.5d correspond to the RF alternating bSSFP sequence applied using the shifted RF excitation frequency, $f_2 = f_1 + 50$ Hz. Banding artifacts in the magnitude images, characterized by loss of signal, are shown by white arrows (Figures 3.5a and 3.5b). It is observed that, as expected, banding artifacts lie in the iso-B_0 lines in both images (refer to the B_0 map in Figure 3.6b). In the phase maps, as shown in Figures 3.5c and 3.5d, a phase shift of π radians is observed in the banding

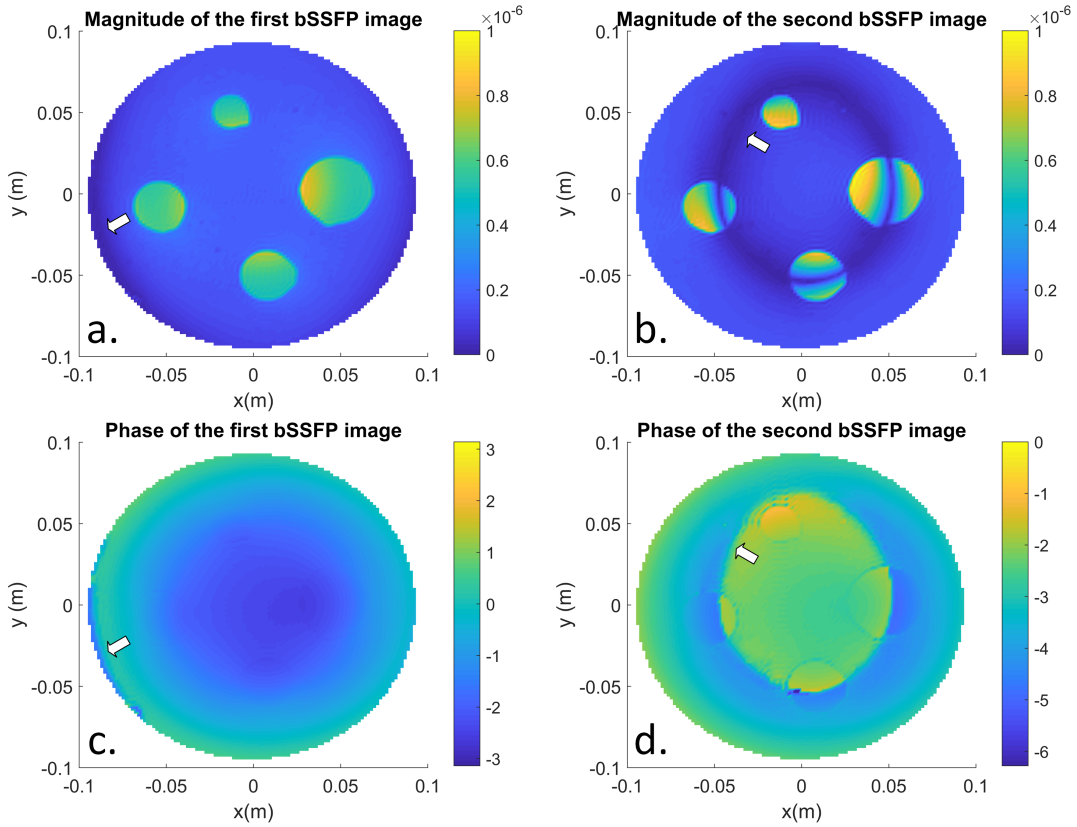

Figure 3.5: For the phantom experiment, **(a-b)** magnitude and **(c-d)** phase images obtained by the two bSSFP sequences. In all images banding artifacts are shown by white arrows.

artifact region. This shift is not phase-wrapping, because it occurs along several pixels as opposed to phase-wrapping which occurs in a single pixel transition by an amount of 2π.

T_2 and B_0 maps for the first phantom are shown in Figure 3.6. It is found that T_2 values are 70 ms and 850 ms, on the average, for the background and anomaly regions respectively. B_0 map demonstrates that there are deviations from central frequency, from -70 Hz to 30 Hz, indicating the extent of B_0 inhomogeneity. The pass-band segments, which are determined by using the B_0 map, are shown in Figure 3.6c. Cyan region corresponds to pixels which are away from banding regions in the first image and the yellow region corresponds to pixels which are away from banding regions in the second image. Putting it differently, cyan region corresponds to pixels which fall in the pass-band segment of the first bSSFP

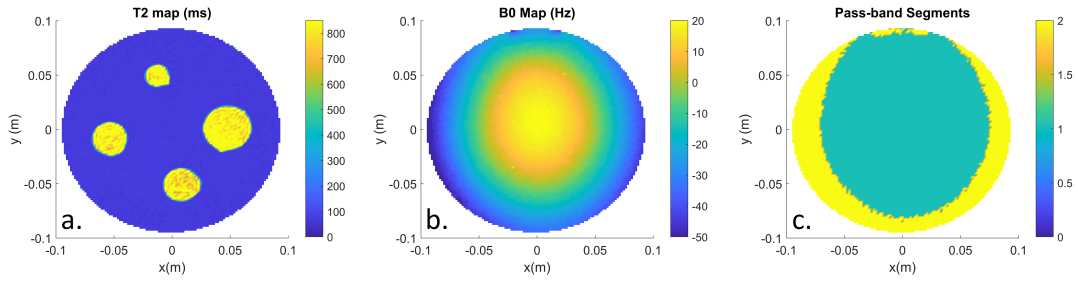

Figure 3.6: For the phantom experiment, **(a)** T_2 map, **(b)** B_0 map, and **(c)** the pass-band segments which are determined based on the B_0 map of the phantom.

experiment and yellow region corresponds to the pass-band segments of the second bSSFP experiment.

The phase of the collaged image, Type-I corrected phase, and Type-II corrected phase image for the first phantom experiment are shown in Figure 3.7a-c. Note that, the phase jumps (for an amount of π) which are observed in the collaged image are corrected in the Type-I corrected phase images as expected. Moreover, phase errors due to finite T_2 values ($E_2 < 1$, non-constant plateau effect) are also corrected for in the Type-II corrected phase image. In order to appreciate the extent of the correction based on T_2 values, Figure 3.7d shows the difference of Type-II corrected phase image and Type-I corrected phase image. The range of the difference image is about $\pm$ 0.06 radians ($\pm$ 3.5 degrees). Phase differences between Type-I and Type-II corrections are largest near the band transition boundaries and also discontinuous across them. In the error map (Figure 3.7d), in the anomalies it is found that phase error is small and this is due to the fact that they have large T_2 values (Figure 3.6a). Although the phase errors between Type-I and Type-II corrected images may be considered to be small for many applications, it will be shown below that use of Type-II correction is essential especially when conductivity reconstruction are considered.

Figure 3.7e displays the expected (theoretical) phase differences between Type-I and Type-II corrections as a function of T_2 and B_0, as calculated by using Equations 3.6 and 3.8. A phase difference does not occur if ΔB_0 is 0 or a multiple of 1/2TR (as also shown in Figure 3.3). It is also observed that phase difference between Type-I and Type-II corrections are largest near the boundaries between

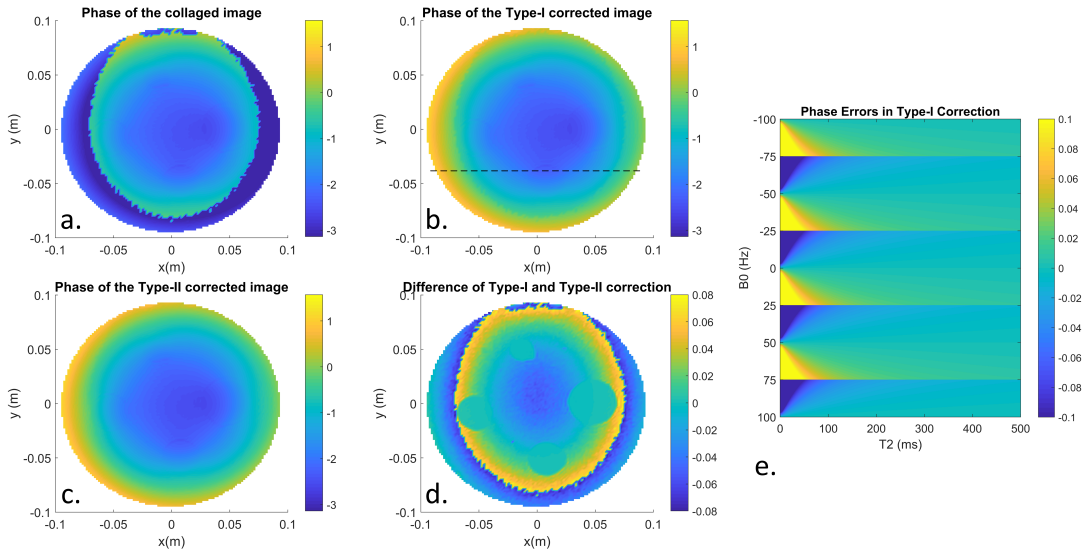

Figure 3.7: For the phantom experiment, **(a)** phase of the collaged image, **(b)** phase of the Type-I corrected image, **(c)** phase of the Type-II corrected image, **(d)** difference between Type-I and Type-II images, and **(e)** theoretical difference between Type-I and Type-II corrected phases as a function of B_0 and T_2. The dotted line in (b) indicates the position of the profile plots shown in Figure 3.9. The unit of phase in all images is radians.

pass-band and stop-band regions and also discontinuous across them. The reason why the error is largest near the boundaries between pass-band and stop-band regions is at these boundaries ΔB_0 corresponds to $\frac{1}{4TR} + \frac{n}{2TR}$ where n is an integer, and these are the off-resonance frequencies at which T_2 has maximal effect. Discontinuity of the error occurs because of the fact that T_2 contribution to phase error, $\angle M$, changes sign across the boundary. With similar reasoning discontinuity of the error in Figure 3.7d is due to the fact that pixels on either sides of the phase transition boundary are taken from different bSSFP images and therefore T_2 contributions to phase error, $\angle(M)$, has opposite polarities across the boundary.

For the first phantom experiment, conductivity maps that are obtained from uncorrected (original) bSSFP phase images using the phase-based cr-MREPT technique are shown in Figures 3.8a and 3.8b. Severe conductivity artifacts occur in the banding artifact regions in both figures even in regions where banding artifact is not fully onset. When the Type-I corrected phase image is used for

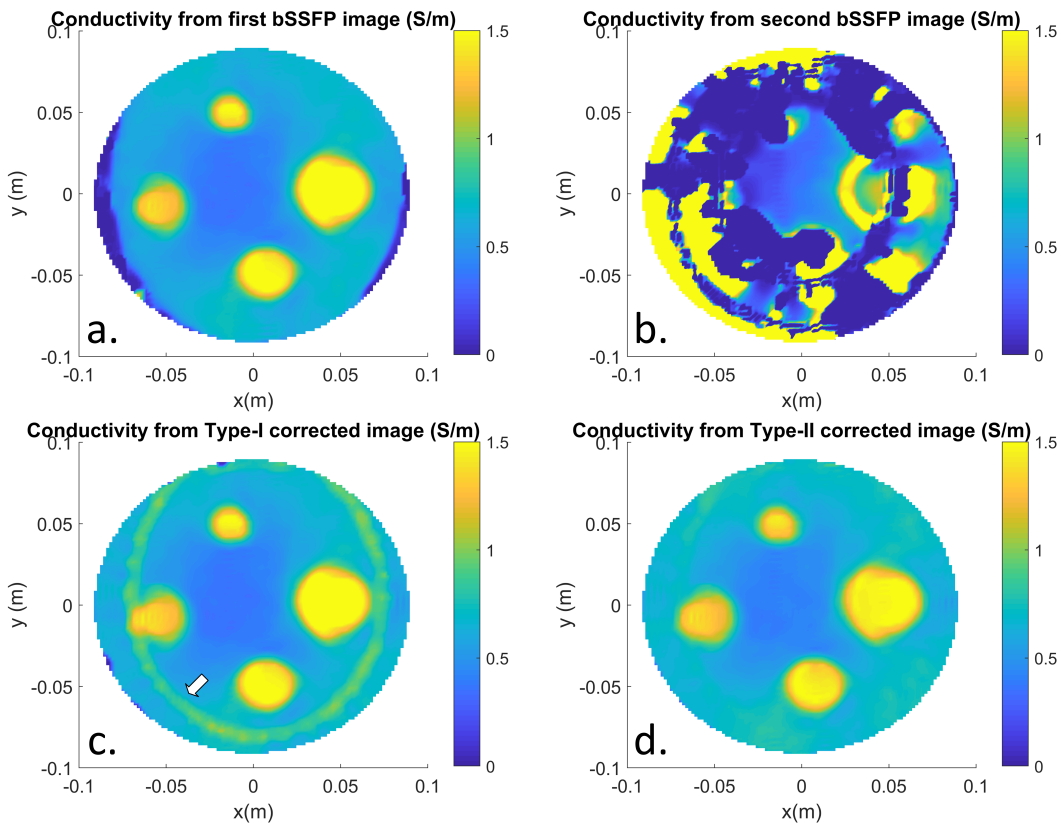

Figure 3.8: For the phantom experiment, **(a)** conductivity map obtained from the phase image of the first bSSFP, **(b)** conductivity map obtained from the phase image of the second bSSFP, **(c)** conductivity map obtained from Type-I corrected image and **(d)** conductivity map obtained from Type-II corrected image. The ring artifact shown in (c) by an arrow is due to the phase ripple observed along the band transition boundary as shown in Figure 3.9.

conductivity reconstruction, significant improvement in the conductivity image is obtained as shown in Figure 3.8c. However, in this case, there is still distortion in the conductivity reconstruction along the band transition boundaries (the ring artifact shown in Figure 3.8c). Although phase errors in Type-I are small, they still distort the conductivity image, since their effects are amplified by Laplacian operation. Nonetheless, when the Type-II corrected phase image is used to reconstruct the conductivity, all artifacts are eliminated and a clean conductivity map is obtained (Figure 3.8d).

Figure 3.9a and 3.9b represent the Type-I and Type-II corrected phase images drawn as 3D surface plot in first phantom experiment. Small phase deviations

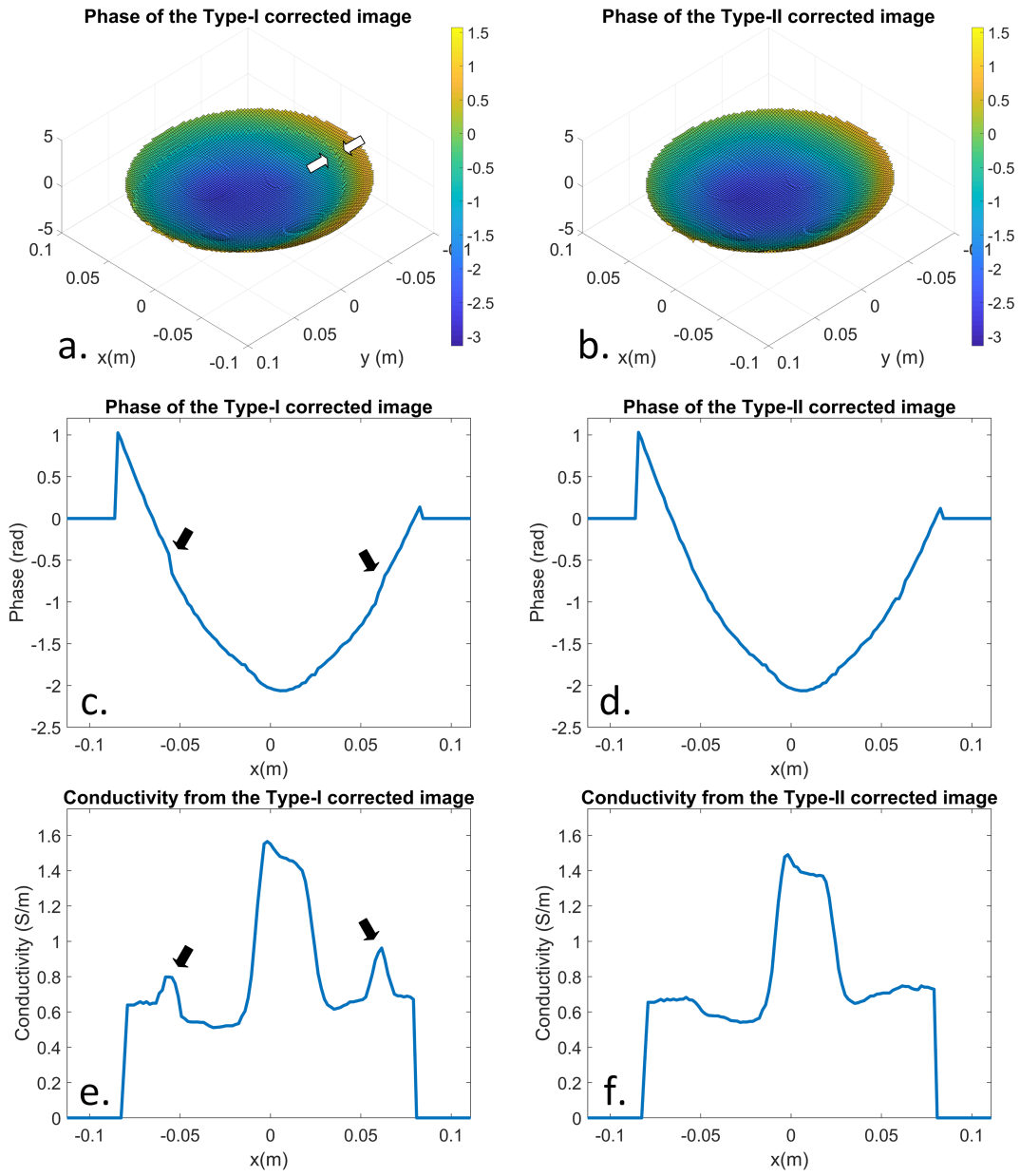

Figure 3.9: For the phantom experiment, **(a)** phase of the Type-I corrected image drawn as 3D surface plot, **(b)** phase of the Type-II corrected image drawn as 3D surface plot, **(c)** phase profile of the Type-I corrected image, **(d)** phase profile of the Type-II corrected image, **(e)** conductivity profile of the Type-I corrected image, and **(f)** conductivity profile of the Type-II corrected image. The profiles are drawn along the line depicted in Figure 3.7b.

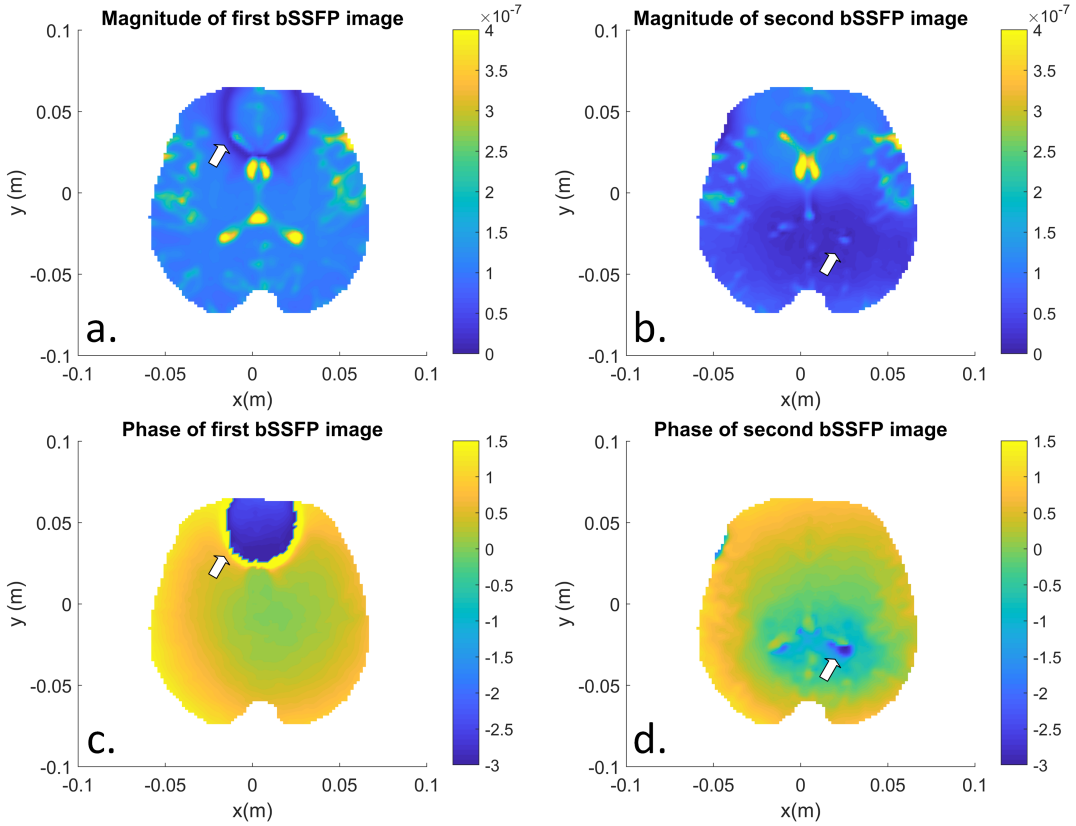

Figure 3.10: For the human experiment, **(a)** magnitude and **(b)** phase images of the first bSSFP sequence, **(c)** magnitude and **(d)** phase images of the second bSSFP sequence. Banding artifacts are shown by white arrows.

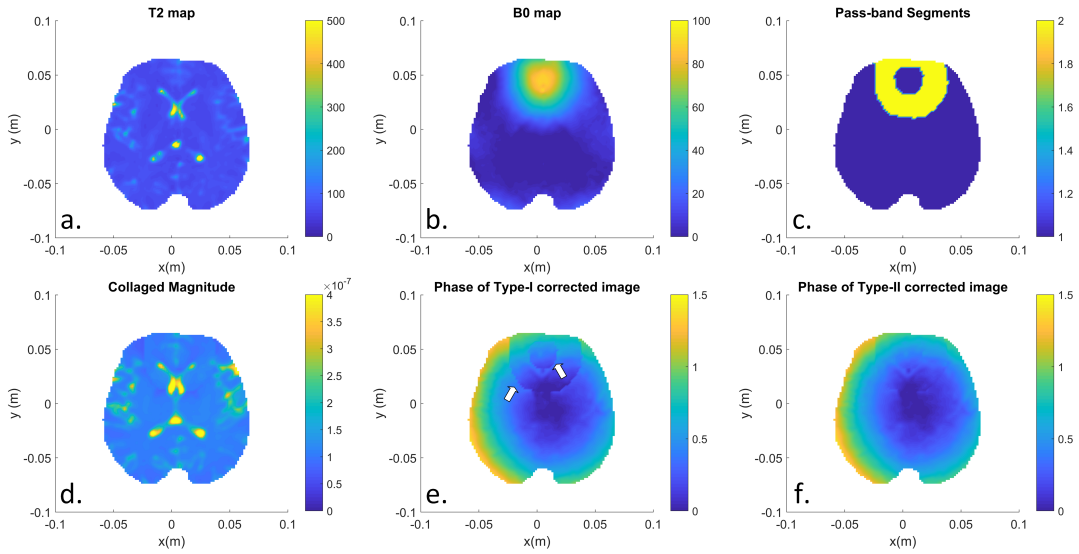

Figure 3.11: For the human experiment, **(a)** T_2 map, **(b)** B_0 map, **(c)** the images of the pass-band segments which are determined based on B_0 map, **(d)** collaged magnitude, **(e)** phase of the Type-I corrected image, and **(f)** phase of the Type-II corrected image. Small phase ripples at the band transition boundary are shown by white arrows.

near the band transition boundaries, in Type-I corrected phase images, are visible in Figure 3.9a and are shown by white arrows. Along the line which is depicted in Figure 3.7b, profiles for phase (Figures 3.9c and 3.9d) and conductivity (Figures 3.9e and 3.9f) for both Type-I and Type-II corrections are shown. Both the small phase deviations and the conductivity ripples corresponding to the band transition boundaries are shown by black arrows (Figures 3.9c and 3.9e). Clearly, when Type-II corrected phase images are used, ripples in the conductivity errors are significantly reduced.

Human experiment results are shown in Figures 3.10, 3.11, 3.12. Figure 3.10 demonstrates the magnitude and phase of both bSSFP runs for a middle axial slice. Banding artifacts are shown by white arrows. T_2 map, B_0 map, pass-band segments, for the same slice, are shown in Figures 3.11a-c. Collaged magnitude is shown in Figure 3.11d. Type-I and Type-II corrected phase images are shown in Figures 3.11e and 3.11f. While Type-I corrected phase image suffers from the small deviations and jumps due to non-constant plateau effect (shown by white arrows), those errors are eliminated in the Type-II corrected phase image. 3D

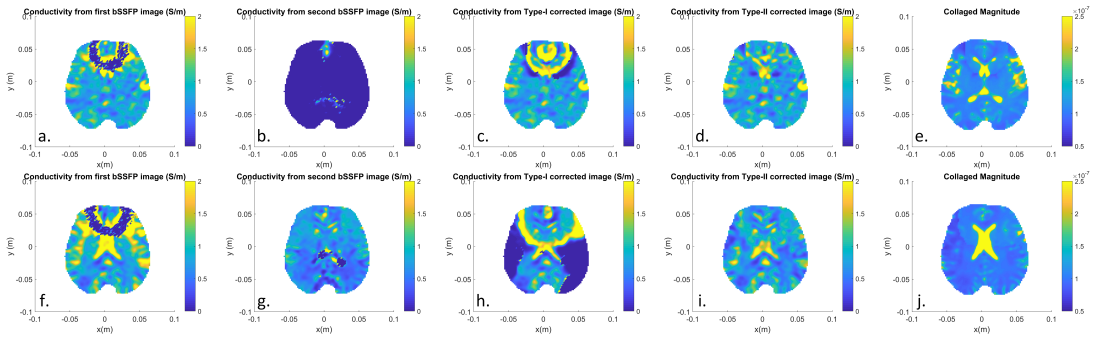

Figure 3.12: For the human experiment, reconstructed conductivities for two different slices of the brain are shown. For the first slice, **(a)** Conductivity map obtained from the first bSSFP phase image, **(b)** conductivity map obtained from the second bSSFP phase image, **(c)** conductivity map obtained from Type-I corrected phase image, **(d)** conductivity map obtained from Type-II corrected phase image, and **(e)** collaged magnitude image. **(f,g,h,i,j)** are the corresponding images for the second slice. Although (a,b,f,g) suffer from banding artifact, (c,h) suffer from non-constant plateau effect, (d,i) are free from such disturbances.

version of phase-based cr-MREPT is used to obtain conductivity maps for 10 slices, and two different slices are shown in Figure 3.12. Due to banding artifact, there are severe distortions on conductivity maps ontained from both bSSFP runs (Figures 3.12a, 3.12b, 3.12f, and 3.12g), and the effect of the non-constant plateau is seen in Figures 3.12c and 3.12h, but conductivity images that are obtained from Type-II corrected phase (Figures 3.12d and 3.12i) do not include such distortions. Collaged bSSFP magnitudes for the two slices are also shown (Figures 3.12e and 3.12j) for comparison with the reconstructed conductivity images.

3.3.2 Linearization for Off-Resonance Estimation - Gauss-Newton Nonlinear Search (LORE-GN) Algorithm

For the second phantom, magnitude and phase of the phantom images obtained by 16 phase-cycled bSSFP images are shown in Figures 3.13 and 3.14, respectively. RF phase increments are selected as $180^\circ - n \cdot 22.5^\circ$ where $n = 0, 1, ..., 15$. As expected, towards the middle of the series of phase-cycled images (especially 9^{th} image), banding artifact becomes prominent as banding artifact manifests itself

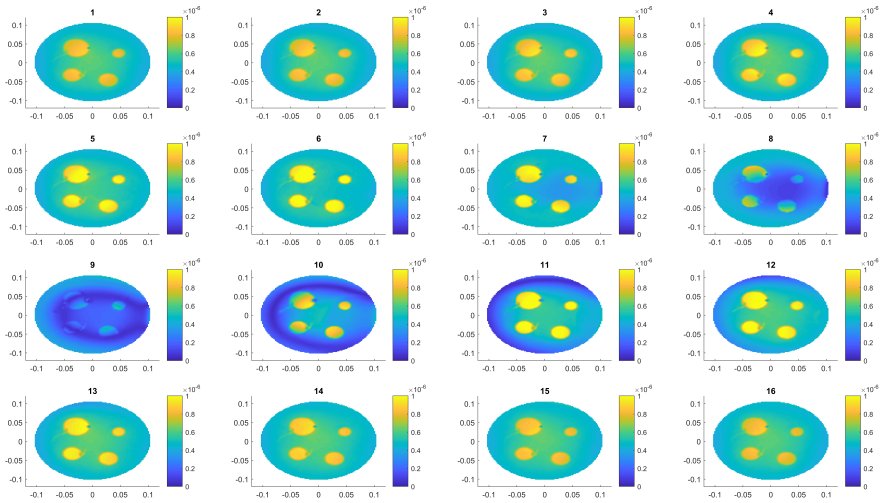

Figure 3.13: Magnitudes of the 16 phase-cycled bSSFP images

via magnitude dips and phase jumps with an amount of π.

Figure 3.15 depicts reconstructed banding-free magnitude image, B_0 map, RF phase, T_2 map which are obtained via LORE-GN algorithm using 16 phase-cycled images. B_0 distribution throughout the object is between [-25, 10] Hz while T_2 values are 180 and 43 ms for anomaly and background regions, respectively. It can be seen that, banding areas in Figures 3.13 and 3.14 are located at iso-B_0 (Figure 3.15b) areas.

Since Equation 3.14 has 6 unknowns and each measurement brings two equations (one for real part, one for imaginary part of the steady state bSSFP complex signal equation), LORE-GN algorithm needs at least 3 different phase-cycled images to reconstruct B_0, T_2, M_{eff} and RF phase. However, increasing the number of phase-cycled images yields high SNR images. It is because of introducing new equations to Equation 3.14 and this has a similar effect with averaging. The effect of using different numbers of phase-cycled images to obtain conductivity maps can be seen in Figure 3.16. Using only one phase-cycled image (without using LORE-GN algorithm) leads to noisy conductivity maps, while increasing the number of used phase-cycled images and implementation of LORE-GN algorithm produce conductivity maps with high SNR.

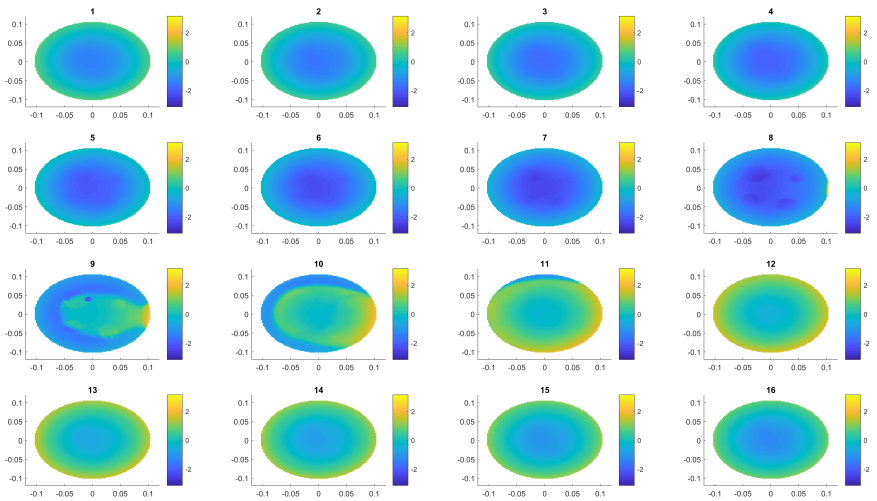

Figure 3.14: Phases of the 16 phase-cycled bSSFP images

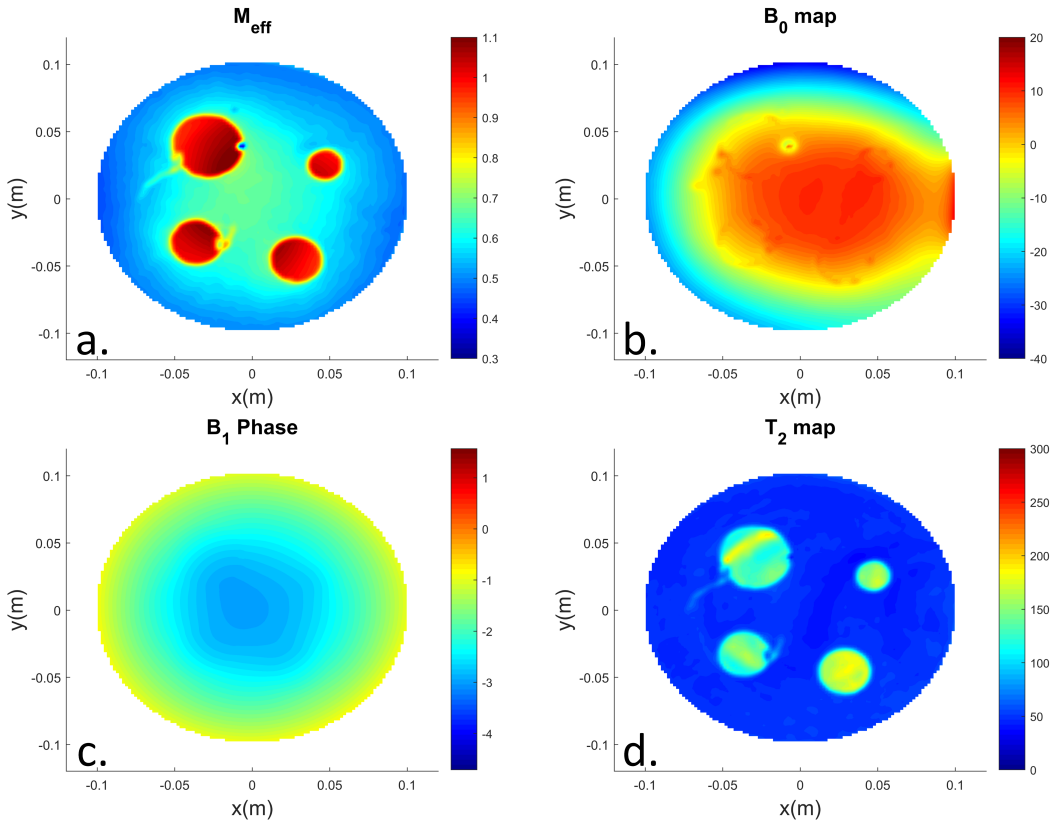

Figure 3.15: **(a)** Reconstructed magnitude image, **(b)** B_0 map, **(c)** RF phase, **(d)** T_2 map obtained by using LORE-GN algorithm

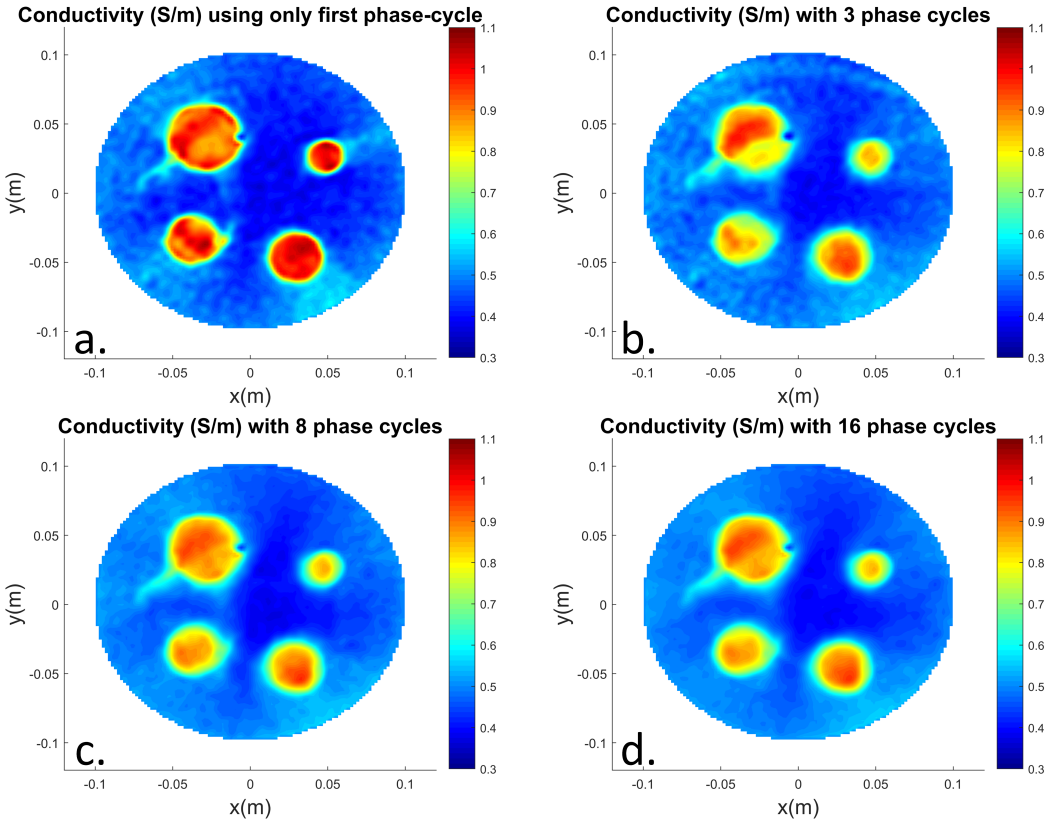

Figure 3.16: Conductiviy maps obtained by using **(a)** first bSSFP phase-cycled image (without using LORE-GN algorithm), **(b)** using 3 phase-cycled images (corresponds to 4^{th}, 9^{th}, and 14^{th} phase-cycled images in Figure 3.14), **(c)** using 8 phase-cycled images (corresponds to 1^{st}, 3^{rd}, 5^{th}, 7^{th}, 9^{th}, 11^{th},13^{th}, and 15^{th} phase-cycled images in Figure 3.14), **(d)** using 16 phase-cycled images

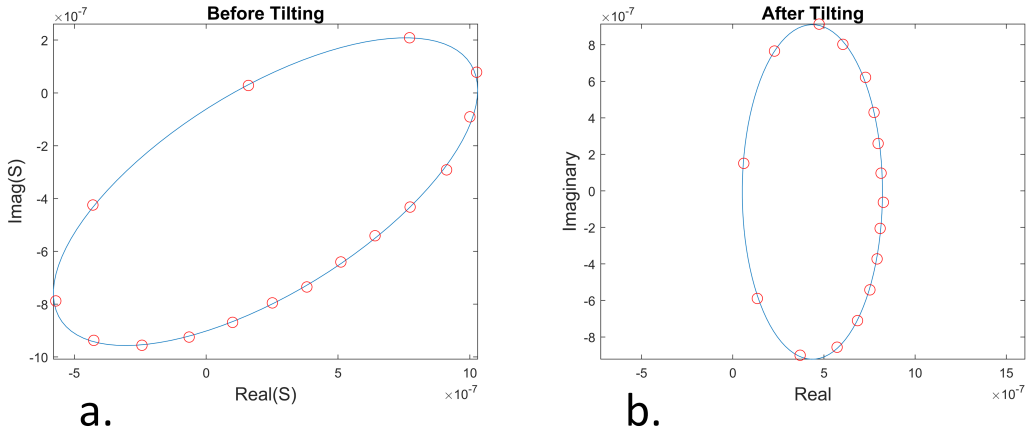

Figure 3.17: With 16 data points, ellipse fitting is shown. **(a)** Before tilting and **(b)** after tilting

3.3.3 PLANET Method

Similar with LORE-GN algorithm, PLANET method uses 16 different phase-cycled bSSFP images with RF phase increments of $180° - n \cdot 22.5°$ where $n = 0, 1, ..., 15$. After that, for each pixel, 16 points (one point for each phase-cycle) are fitted into an ellipse. This fitting is shown in Figure 3.17a. After fitting, φ_{rot} is eliminated and tilted ellipse is obtained (Figure 3.17b). Note that, right side of the ellipse has more points than the left side. This is because pixels on the right side lies within the pass-band region where phase changes almost linearly and slowly, while pixels on the left side lies within the stop-band region where phase changes drastically with RF phase increments.

Figure 3.18 depicts reconstructed banding-free magnitude image, B_0 map, RF phase, and T_2 map which are obtained by PLANET method using 16 phase-cycled images for the second phantom. B_0 distribution through image is between [-25, 10] Hz while T_2 values are 190 and 50 ms for anomaly and background regions, respectively. It can be seen that, banding areas in Figures 3.13 and 3.14 are located at iso-B_0 (Figure 3.18b) areas.

Figure 3.19 shows two sets of 16 phase-cycled images which are acquired successively (blue points are obtained first, red ones are obtained afterwards). As

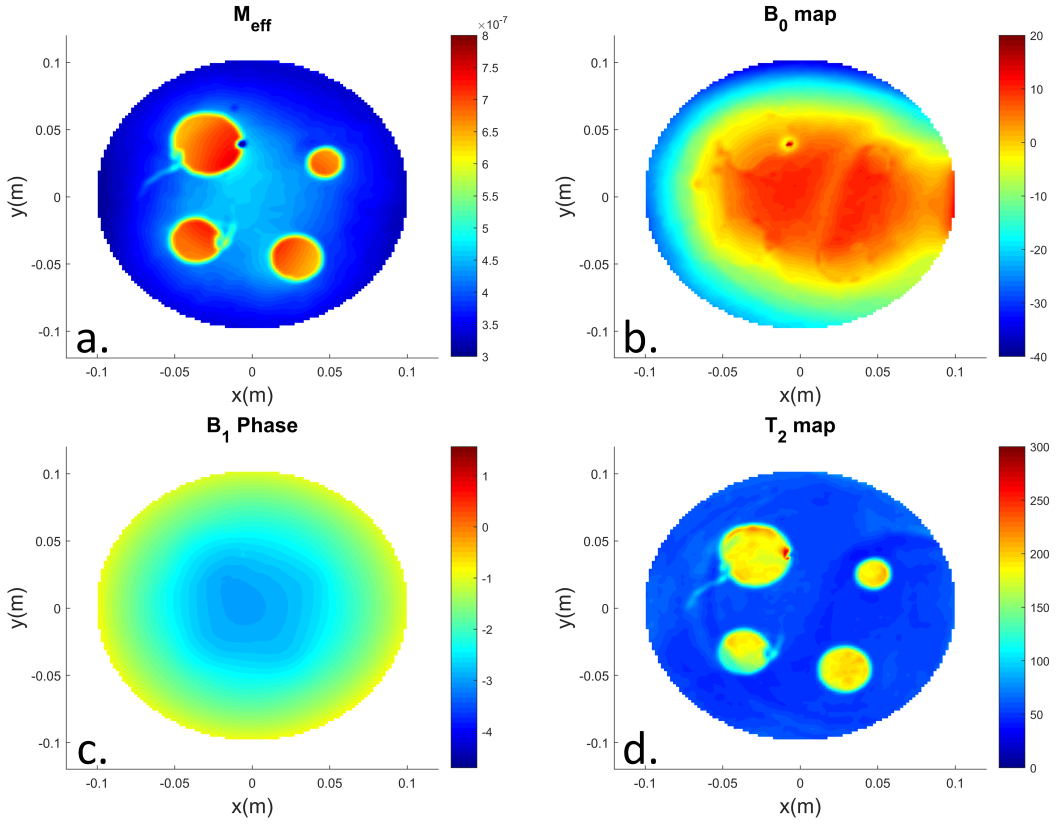

Figure 3.18: **(a)** Reconstructed magnitude image, **(b)** B_0 map, **(c)** RF phase, **(d)** T_2 map obtained by using PLANET method

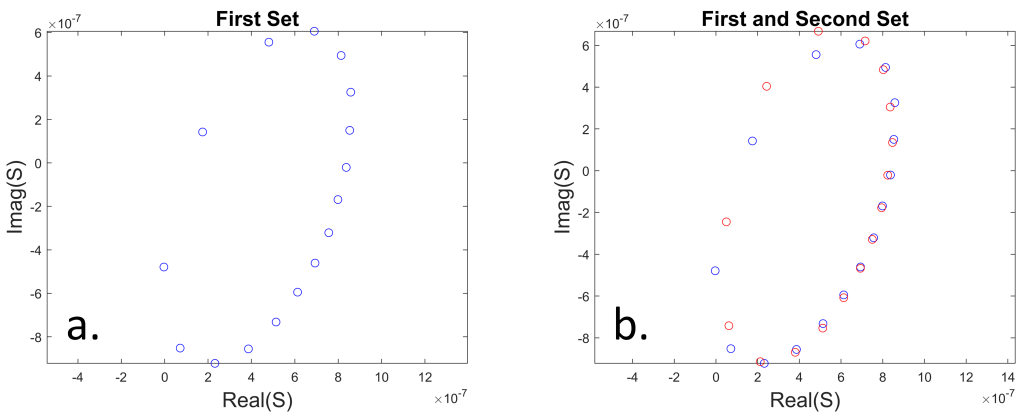

Figure 3.19: **(a)** First set of 16 phase-cycled bSSFP image **(b)** First and second sets of 16 phase-cycled bSSFP image are shown

seen, although points that are located on the right side of the ellipse are matched, there are huge variations on the points on left side of the ellipse. The reason of this is that points which are located on the left side of the ellipse are close to the banding artifact and when banding artifact occurs, complex image values become very sensitive to the B_0 changes (see Figure 3.2). Therefore, in case of any B_0 disturbances throughout the scanning, like B_0 drift, points on the left side of the ellipse are distorted drastically, while points on the right side of the ellipse remain almost same. On the other hand, if B_0 change is low, fitted ellipses of two different acquisitions would be same with the exception of relatively small $e^{-i2\pi\Delta f_0 \mathrm{TE}}$ phase term. Therefore, the structure of the ellipse will not be distorted, yet points will be shifted on the ellipse. With the effect of this, T_1, T_2, and M_{eff} images do not deteriorate significantly, since they only depend on the properties of the ellipse (semi-axes and center). However, Δf_0 and RF phase acquisitions are distorted, since they also depend on the each of 16 points seperately.

To obtain θ_0 by using Equation 3.32, normally one should use entire 16 points of phase-cycled bSSFP image set and solve Equation 3.32 in a least squares sense. Yet, since points on left side of the ellipse are not accurate, we can simply ignore them and use only the points that are located on the right side of the ellipse. Figure 3.20 consists of conductivity maps that are obtained by using all of the 16 phase-cycled bSSFP images (Figure 3.20b) and by using only 8 points that are located on the right side of the ellipse (Figure 3.20a). Although Figure 3.20b is

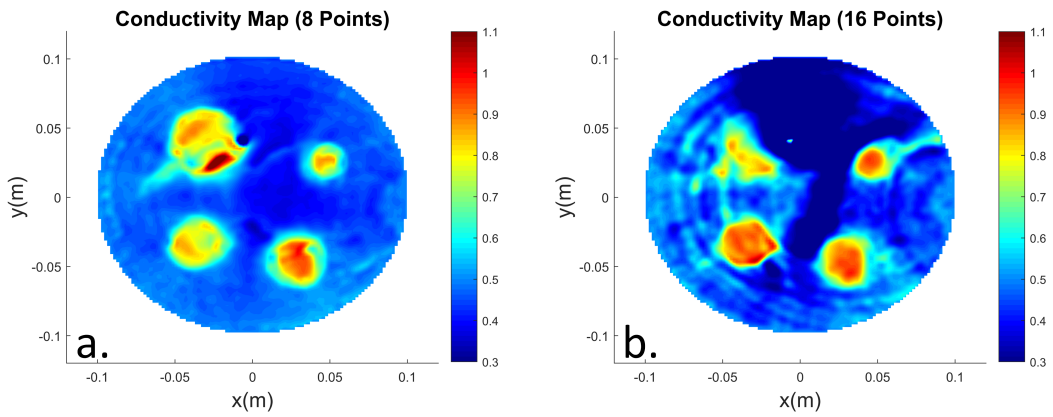

Figure 3.20: Conductivity images are shown which is obtained **(a)** by using 8 points on the right side of the ellipse and **(b)** by using all of the 16 points

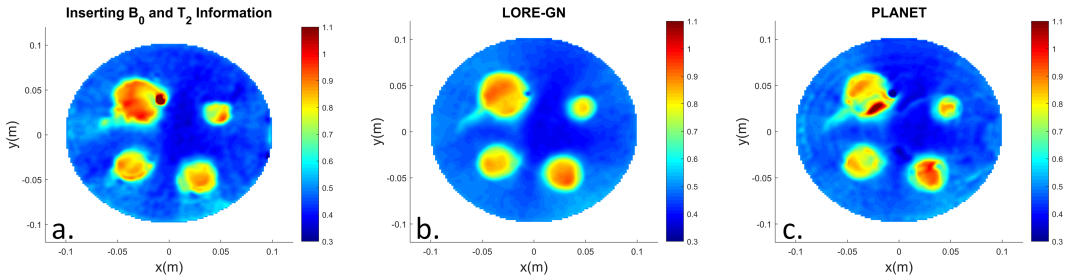

Figure 3.21: Conductivity maps obtained by **(a)** inserting B_0 and T_2 information, **(b)** using LORE-GN algorithm, and **(c)** using PLANET method.

distorted by points on the left side of the ellipse, Figure 3.20a does not have such distortions and it depicts conductivity map clearly.

Conductivity maps obtained from all aforementioned bSSFP phase correction methods for the second phantom is shown in Figure 3.21. By visual inspection, LORE-GN algorithm can be regarded as the best correction method for bSSFP phase images.

3.4 Discussion and Conclusions

It has been argued that bSSFP is the most favourable phase measuring method for MREPT because of its speed, motion insensitivity, automatic eddy current

compensation and high SNR [19,25]. However, bSSFP phase is susceptible to off-resonance and T_2 effects, and it is vulnerable especially in certain regions where banding artifact occurs. In this chapter, this issue is addressed and three different correction methods for obtaining correct RF phase throughout the object are analyzed. It has also been shown that, those correction methods provide phase distributions which have sufficient quality for obtanining conductivity images.

For the first method (inserting B_0 and T_2 information), acquisition time is high, due to the selection of reliable but lenghty B_0 and T_2 mapping methods. Though methods that use phase-cycled bSSFP imaging decrease acquisiton time significantly, one needs to investigate the usage of them thoroughly. For example, PLANET method suffers from B_0 drift and also propagation of error. The reason of the latter is to obtain RF transceive phase, one needs to estimate T_1, T_2 and M_{eff} first, then estimate B_0 and RF phase. In each step, error causes more disturbed RF transceive phase images, and that leads to erroneous conductivity maps. Therefore, it is found that using LORE-GN algorithm is favourable, since it requires only 3 phase-cycled bSSFP images (in comparison to PLANET method, that requires 6 phase-cycled bSSFP images), and it finds RF phase in a single step.

Chapter 4

B_1 Magnitude Imaging Methods and their use in MREPT

4.1 Theory of B_1 Magnitude Mapping Methods

4.1.1 Double Angle (DA) Method

Double angle method is first suggested by Stollberger [30]. The signal intensity, I, of a spin-echo sequence at an arbitrary pixel can be described as:

$$I = k\,\rho\,S\,\sin(\alpha)\,\sin^2\left(\frac{\beta}{2}\right)R_1(\alpha,\,\beta,\,\mathrm{TR},\,\mathrm{TE},\,\mathrm{T_1})e^{-\mathrm{TE/T_2}} \tag{4.1}$$

where TE and TR represent echo time and repetition time, α is excitation angle, β is refocussing angle, ρ is spin density, k is system constant, S is coil sensitivity and $R_1(\alpha,\,\beta,\,\mathrm{TR},\,\mathrm{TE},\,\mathrm{T_1})e^{-\mathrm{TE/T_2}}$ corresponds to longitudinal relaxation. If we use two different flip-angles, α_1 and α_2, ratio of corresponding signal intensities, I_1/I_2 can be written as:

$$\frac{I_1}{I_2} = \frac{\sin(\alpha_1)}{\sin(\alpha_2)} \cdot \frac{R_1(\alpha_1,\,\beta,\,\mathrm{TR},\,\mathrm{TE},\,\mathrm{T_1})e^{-\mathrm{TE/T_2}}}{R_1(\alpha_2,\,\beta,\,\mathrm{TR},\,\mathrm{TE},\,\mathrm{T_1})e^{-\mathrm{TE/T_2}}} \tag{4.2}$$

By using repetition time as $\mathrm{TR} \geq 5\mathrm{T}_{1,max}$, the longitudinal relaxation terms will be equal to each other and the ratio depends only on the flip-angles, α_1 and α_2

respectively. If α_2 is selected as $\alpha_2 = 2\alpha_1$, α_1 can be found as:

$$\alpha_1 = cos^{-1}\left(\frac{I_2}{2I_1}\right) \tag{4.3}$$

4.1.2 Actual Flip-Angle Imaging (AFI) Method

Actual flip-angle imaging method is first suggested by Yarnykh [31]. In this method, two identical RF pulses are used with different TRs (Figure 4.1). After each RF pulse, signal is acquired by using gradient-echo scheme. With assumptions of both TRs are less than T_1 and spoiling is ideally done, in steady state, longitudinal magnetization before each excitation can be written as:

$$\begin{aligned} M_{z1} &= M_0 \frac{1 - E_2 + (1 - E_1)E_2 \cos(\alpha)}{1 - E_1 E_2 \cos^2(\alpha)} \\ M_{z2} &= M_0 \frac{1 - E_1 + (1 - E_2)E_1 \cos(\alpha)}{1 - E_1 E_2 \cos(\alpha)} \end{aligned} \tag{4.4}$$

where $E_{1,2} = e^{-\mathrm{TR}_{1,2}/\mathrm{T}_1}$ and M_0 is the equilibrium magnetization. With the addition of T_2 and excitation effects, observed signals become:

$$S_{1,2} = M_{z1,2} e^{-\mathrm{TE}/\mathrm{T}_2} \sin(\alpha) \tag{4.5}$$

and their ratio is:

$$r = S_2/S_1 = \frac{1 - E_1 + (1 - E_2)E_1 \cos(\alpha)}{1 - E_2 + (1 - E_1)E_2 \cos(\alpha)} \tag{4.6}$$

By using first order Taylor series expansion ($e^{-x} = 1 - x$) and short TR_1 and TR_2 values, this ratio can be approximated as:

$$r \approx \frac{1 + n\, cos(\alpha)}{n + cos(\alpha)} \tag{4.7}$$

where $n = \mathrm{TR}_2/\mathrm{TR}_1$. Then, α can be found as:

$$\alpha \approx \cos^{-1} \frac{rn - 1}{n - r} \tag{4.8}$$

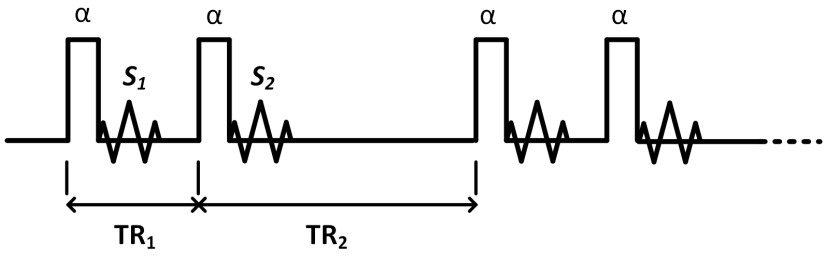

Figure 4.1: Pulse sequence diagram of the AFI

4.1.3 Bloch-Siegert Shift based Method

Bloch-Siegert shift based method is first suggested by Sacolick [32]. In this method, unlike previous methods, B_1 information is encoded into signal phase, rather than its magnitude. In order to obtain B_1 information, after the excitation pulse, an RF pulse with off-frequency is applied in order to cause Bloch-Siegert shift (Figure 4.2). The frequency difference between resonance frequency and second RF pulse is ω_{RF}. Effective RF pulse becomes:

$$\gamma B_1^{eff} = \sqrt{\omega_{RF}^2 + \gamma B_1^2} \tag{4.9}$$

By using such an RF pulse, Bloch-Siegert shift, ω_{BS} emerges. When $\omega_{RF} >> \gamma B_1$, this shift is along approximately with the main magnetic field. Under the assumption of $\omega_{RF} >> \gamma B_1$, pythagorean equation becomes (Figure 4.3):

$$\begin{aligned} (\omega_{BS} + \omega_{RF})^2 &= \omega_{RF}^2 + (\gamma B_1)^2 \\ \omega_{BS} &\approx \frac{(\gamma B_1)^2}{2\omega_{RF}} \end{aligned} \tag{4.10}$$

Including off-resonance effect to Equation 4.10, ω_{BS} becomes:

$$\omega_{BS} = \frac{(\gamma B_1)^2}{2(\omega_{RF} + \omega_{B0})} \tag{4.11}$$

By using second order Taylor expansion with the assupmtion of $\omega_{B0} << \omega_{RF}$:

$$\omega_{BS} = \frac{(\gamma B_1)^2}{2(\omega_{RF} + \omega_{B0})} \approx \frac{(\gamma B_1)^2}{2\omega_{RF}} - \frac{(\gamma B_1(t))^2 \omega_{B0}}{2\omega_{RF}^2} + O(\omega_{B0}^2) \tag{4.12}$$

After that, phase shift caused by Bloch-Siegert shift can be found as:

$$\phi_{BS} = \int_0^T \omega_{BS} dt = \int_0^T \frac{(\gamma B_1(t))^2}{2\omega_{RF}(t)} dt - \int_0^T \frac{(\gamma B_1(t))^2 \omega_{B0}}{2\omega_{RF}^2} dt + O(\omega_{B0}^2) \tag{4.13}$$

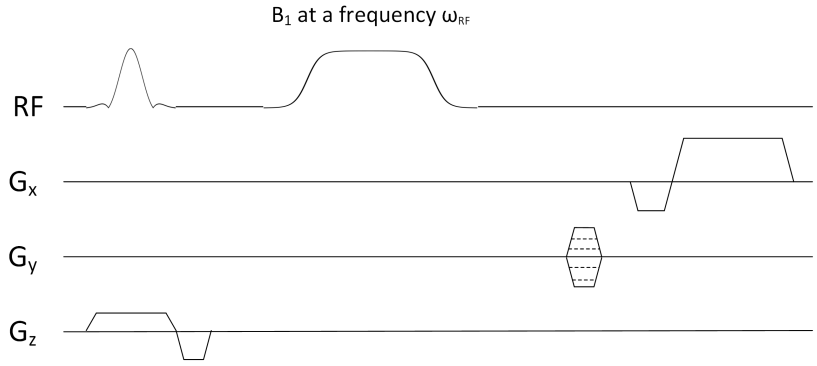

Figure 4.2: Pulse sequence diagram of the Bloch-Siegert shift based method

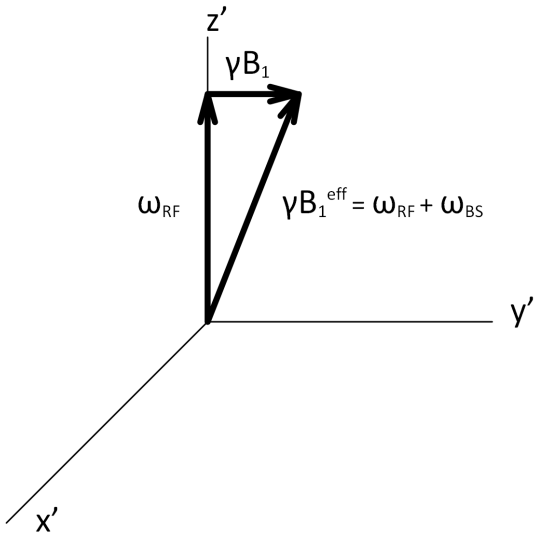

Figure 4.3: RF pulse of Bloch-Siegert shift based method in the rotating frame

There is a B_0 dependency of the second term. This term can be eliminated by using two scans with symmetric off-resonance pulses as $\pm\omega_{RF}$. Taking the phase difference will cancel the second term and thus ϕ_{BS} will be independent of B_0:

$$\phi_{BS} = \int_0^T \frac{(\gamma B_1(t))^2}{2\omega_{RF}(t)} dt = B_{1,peak}^2 \int_0^T \frac{(\gamma B_{1,normalized})^2}{2\omega_{RF}(t)} = B_{1,peak}^2 \cdot K_{BS} \quad (4.14)$$

Therefore,

$$B_{1,peak} = \sqrt{\frac{\phi_{BS}}{K_{BS}}} \quad (4.15)$$

K_{BS} is constant and related to the RF pulse shape, $B_{1,peak}$ is the peak magnitude of the B_1.

4.2 SNR Calculations of B_1 Magnitude Mapping Methods

These SNR calculations are made by Omer Faruk Oran. These calculations can also be found in progress reports of the TÜBİTAK project (114E522).

4.2.1 Double Angle Method

In this method, we obtain two different image, S_1 and S_2 by using different flip angles, α_1 and 2α. PDF of their ratios ($r = S_1/S_2$) can be written as [41]:

$$f_R(r) = \frac{(rS_1 + S_2)}{\sigma\sqrt{2\pi}(r^2+1)^{3/2}}\exp\left(-\frac{(r - S_1/S_2)^2}{2\sigma^2(r^2+1)/S_2^2}\right)\mathrm{erf}\left(\frac{rS_1 + S_2}{\sigma\sqrt{2(r^2+1)}}\right) + \frac{1}{\pi(r^2+1)}\exp\left(-\frac{S_1^2 + S_2^2}{2\sigma^2}\right) \tag{4.16}$$

With the assumption of both $\mathrm{SNR}_1 = S_1/\sigma$ and $\mathrm{SNR}_2 = S_2/\sigma$ is greater than 3, Equation 4.16 can be simplified as:

$$f_R(r) = \frac{(rS_1 + S_2)}{\sigma\sqrt{2\pi}(r^2+1)^{3/2}}\exp\left(-\frac{(r - S_1/S_2)^2}{2\sigma^2(r^2+1)/S_2^2}\right) \tag{4.17}$$

By using $\alpha = g(r) = \cos^{-1}(1/2r)$, PDF of the flip angle can be found as:

$$\begin{aligned} f_A(\alpha) &= \frac{f_R(g^{-1}(\alpha))}{|\frac{dg(g^{-1}(\alpha))}{dr}|} = \frac{\sin\alpha}{2\cos^2\alpha} f_R(1/2\cos\alpha) \\ &= \frac{\sin\alpha}{2\cos^2\alpha}\frac{4\cos^2\alpha(S_1 + 2\cos\alpha S_2)}{\sigma\sqrt{2\pi}(1+4\cos^2\alpha)^{3/2}}\exp\left(-\frac{(S_2 - 2\cos\alpha S_1)^2}{2\sigma^2(1+4\cos^2\alpha)}\right) \end{aligned} \tag{4.18}$$

The term that causes rapid changes in PDF is the nominator in the exponential term, $(S_2 - 2\cos\alpha\, S_1)^2/2\sigma^2$. When we have high SNR_1 and SNR_2, we can use second order Taylor expansion around expected flip angle, α_0, as $\cos\alpha \approx \cos\alpha_0 - \sin\alpha_0(\alpha - \alpha_0)$. After this, PDF of the flip angle becomes:

$$f_A(\alpha) \approx \frac{1}{\sigma^*\sqrt{2\pi}}\exp\left(-\frac{(\alpha - \alpha_0)^2}{2\sigma^*}\right) \tag{4.19}$$

where

$$\sigma^* = \frac{\sigma\sqrt{1+4\cos^2(\alpha_0)}}{S_1 2\sin(\alpha_0)} = \frac{1}{SNR_1}\frac{\sqrt{1+4\cos^2(\alpha_0)}}{2\sin(\alpha_0)} \tag{4.20}$$

Since $\mathrm{SNR}_1 = \mathrm{SNR}_{90}\sin(\alpha_0)$, where SNR_{90} is the SNR value when flip angle is picked as 90°, standard deviation becomes:

$$\sigma^* = \frac{\sqrt{1+4\cos^2\alpha_0}}{\mathrm{SNR}_{90}\ 2\sin^2\alpha_0} \tag{4.21}$$

Since $\mathrm{SNR} = \frac{\mathrm{mean}(\alpha)}{\sigma}$:

$$\mathrm{SNR} = \mathrm{SNR}_{90}\frac{\alpha_0 2\sin^2\alpha_0}{\sqrt{1+4\cos^2\alpha_0}} \tag{4.22}$$

This formulation holds only if TR is at least $5\mathrm{T}_1$. This limitation led to longer acquisition time in comparison to the faster techniques like actual flip-angle imaging method or Bloch-Siegert shift based method.

4.2.2 Actual Flip-Angle Imaging Method

Flip angle of the AFI is described as:

$$\alpha = g(r) = \cos^{-1}\left(\frac{rn-1}{n-r}\right) \tag{4.23}$$

Similar to Equation 4.18, PDF of the flip angle can be written as:

$$\begin{aligned} f_A(\alpha) &= \frac{f_R(g^{-1}(\alpha))}{|\frac{dg(g^{-1}(\alpha))}{dr}|} = \frac{(n^2-1)\sin\alpha}{(n+\cos\alpha)^2} f_R\left(\frac{1+n\cos\alpha}{n+\cos\alpha}\right) \\ &= \frac{(n^2-1)\sin\alpha}{(n+\cos\alpha)^2}\frac{1}{\sigma'\sqrt{2\pi}}\exp\left(-\frac{(\frac{1+n\cos\alpha}{n+\cos\alpha} - S_1/S_2)^2}{2\sigma'^2}\right) \end{aligned} \tag{4.24}$$

Again, when similar procedure with Equation 4.19 is followed:

$$f_A(\alpha) \approx \frac{1}{\sigma^*\sqrt{2\pi}}\exp\left(-\frac{(\alpha-\alpha_0)^2}{2\sigma^{*2}}\right) \tag{4.25}$$

where

$$\sigma^* = \frac{(n+\cos\alpha_0)\sqrt{r_0+1}}{(n-r_0)\sin\alpha_0}\frac{\sigma}{S_2} = \frac{1}{\mathrm{SNR}_2}\frac{(n+\cos\alpha_0)\sqrt{r_0+1}}{(n-r_0)\sin\alpha_0} \tag{4.26}$$

Since $\mathrm{SNR}_2 = \mathrm{SNR}_{90}\sin\alpha\frac{1-E_2+(1-E_1)E_2\cos\alpha}{1-E_1E_2 cos\alpha}$, Equation 4.26 becomes:

$$\sigma^* = \frac{1}{\mathrm{SNR}_{90}}\frac{(1-E_1E_2\cos^2\alpha_0)(n+\cos\alpha_0)\sqrt{r_0^2+1}}{(1-E_2+(1-E_1)E_2\cos\alpha_0)(n-r_0)\sin^2(\alpha_0)} \tag{4.27}$$

Therefore,

$$\mathrm{SNR} = \mathrm{SNR}_{90}\frac{\alpha_0(1-E_2+(1-E_1)E_2\cos\alpha)(n-r_0)\sin^2\alpha_0}{(1-E_1E_2\cos^2\alpha_0)(n+\cos\alpha_0)\sqrt{r_0^2+1}} \tag{4.28}$$

4.2.3 Bloch-Siegert Shift based Method

With the definitions of B_0^{peak} and $\varphi_{BS,0}$ as expected B_{peak} and φ_{BS}, $\sigma_{B_0^{peak}}$ can be found by using propagation of uncertainty as follows:

$$\sigma_{B_0^{peak}} = \frac{\partial f(\varphi_{BS})}{\partial \varphi_{BS}} \sigma_{\varphi_{BS}} = \frac{1}{2\sqrt{\varphi_{BS,0} K_{BS}}} \sigma_{\varphi_{BS}} \tag{4.29}$$

Since Bloch-Siegert shift based method uses gradient echo-based imaging, which utilizes low TR, complex image amplitude at an arbitrary pixel becomes:

$$S = \frac{M_0(1 - E_1)\sin\alpha}{1 - E_1 - \cos\alpha} e^{-\mathrm{TE}/\mathrm{T}_2} \tag{4.30}$$

Therefore,

$$\mathrm{SNR}_{\varphi_{BS}} = \mathrm{SNR}_{90} \frac{(1 - E_1)\sin\alpha}{1 - E_1 \cos\alpha} \tag{4.31}$$

Therefore, SNR becomes:

$$\mathrm{SNR} = \mathrm{SNR}_{90} \frac{2 K_{BS} {B_0^{peak}}^2 (1 - E_1)\sin\alpha}{1 - E_1 \cos\alpha} \tag{4.32}$$

4.3 Experimental Methods

4.3.1 Phantom Preparation

For SNR calculation of B_1 maps, cylindrical uniform phantom is used. For standard MREPT and cr-MREPT methods, a cylindrical z-independent experimental phantom with diameter of 20 cm and height of 17 cm was constructed. For background region, agar-saline gel (20 g/L agar, 2 g/L NaCL, 1.5 g/L $CuSO_4$) was used, and for anomalies, longitudinal holes were drilled and filled with saline solution (6 g/L NaCL, 1.5 g/L $CuSO_4$). The conductivity values for background and the anomaly regions are expected to be 0.5 and 1 S/m respectively [20]. Anomaly regions have diameters of 0.5, 1.5, and 2.5 cm.

4.3.2 Selection of Parameters

To compare different B_1 mapping techniques, we need to decide different parameters like α_0, TR, K_{BS}... etc.

- Since double angle method does not work around 90° flip angle (2α becomes 180°, therefore second signal vanishes) and actual flip-angle imaging method only works when flip angle is lower than 90° [31], α is chosen as 60° to be on the safe side.
- n parameter in AFI is selected as 5 and TR_1/TR_2 is selected as 30/150 ms as in Yarnkh 2006 [31].
- In line with the previous work [32], TR is picked as 100 ms, B_{peak} is selected as 9 μT, K_{BS} is selected as 5920 rad/(mT)^2 (this corresponds to Fermi pulse with length of 6 ms and off-resonance frequency of 1 kHz).

4.3.3 SNR Calculation of B_1 Magnitude Maps

Assume that, two MR images are obtained identically. Then, for each pixel

$$\begin{aligned} I_1 &= S + n_1 \\ I_2 &= S + n_2 \end{aligned} \tag{4.33}$$

where I_1 and I_2 are obtained image pixels, S is noiseless image pixels and n_1 and n_2 are independent Gaussian white noises with zero mean and same standard deviation, σ. When subtraction is used:

$$I_1 - I_2 = n_1 - n_2 \tag{4.34}$$

Since noises are independent and zero mean: $\sigma^2_{n_1-n_2} = \sigma^2_{n_1} + \sigma^2_{n_2} = 2\sigma^2$. Therefore,

$$\sigma_I = \frac{\sigma_{I_1-I_2}}{\sqrt{2}} \tag{4.35}$$

4.3.4 Sequence Parameters

For calculating SNR of B_1 via double angle method, two gradient echo images with different flip angles are obtained. The sequence parameters in the phantom experiment were: TE/TR = 10/3500 ms, FoV (field of view) = 200 mm, FA (flip angle) = 60° or 120°, slice thickness = 2 mm, number of slices = 1, duration for each average = 14 minutes 57 seconds, number of averages (NEX) = 4. For actual-flip angle imaging method, scan parameters were selected as: TR_1/TR_1 = 30/150 ms, n = 5, FoV = 200 mm, FA = 60°, slice thickness = 2 mm, number of slices = 1, duration for each average = 23 seconds, NEX = 156. For Bloch-Siegert shift based method, scan parameters were selected as: TR = 100 ms, TE = 10 ms, FoV = 200 mm, FA = 60°, slice thickness = 2 mm, number of slices = 1, duration for each average = 26 seconds, NEX = 140.

For calculating SNR of B_1 via double angle method, two gradient echo images with different flip angles are obtained. The sequence parameters in the phantom experiment were: TE/TR = 10/3500 ms, FoV (field of view) = 225 mm, FA (flip angle) = 60° or 120°, slice thickness = 2 mm, number of slices = 1, duration for each average = 14 minutes 57 seconds, NEX = 4. For actual-flip angle imaging method, scan parameters were selected as: TR_1/TR_1 = 30/150 ms, n = 5, FoV = 225 mm, FA = 60°, slice thickness = 2 mm, number of slices = 1, duration for each average = 23 seconds, NEX = 156. For Bloch-Siegert shift based method, scan parameters were selected as: TR = 100 ms, TE = 10 ms, FoV = 225 mm, FA = 60°, slice thickness = 2 mm, number of slices = 1, duration for each average = 26 seconds, NEX = 140. For phase of B_1, 2D bSSFP sequence is used. Scans parameters were: TE/TR = 2.28/4.56 ms, FoV = 225 mm, FA = 40°, slice thickness = 2 mm, number of slices = 1, NEX = 20.

4.4 Results

For the uniform phantom experiment, B_1 maps, which are obtained by using double angle (DA) method, actual flip-angle imaging (AFI) method and Bloch-Siegert shift (BSS) based method, are shown in Figures 4.4, 4.5, and 4.6. Number of averages are picked as 4, 140, and 156 for double angle method, Bloch-Siegert shift based method and actual flip-angle imaging method, respectively, to obtain similar scanning time (approximately 1 hour). For each figure, 2D and 3D surface plots of B_1 maps taken with one average (single acquisition) and one hour scan are shown. Although one average yields noisy B_1 maps in actual flip-angle imaging and Bloch-Siegert shift based methods (Figures 4.5a,c and 4.6a,c) compared to double angle method (Figures 4.4a,c), by using averaging, actual flip-angle imaging and Bloch-Siegert shift based methods (Figures 4.5b,d and 4.6b,d) becomes preferable over double angle method (Figures 4.4b,d), due to their high SNR values.

Theoretical and experimental SNR values for selected parameters with respect to time are shown in Figure 4.7. It is clear that, experimental SNR results are consistent with the theoretical ones. According to Figure 4.7, Bloch-Siegert shift based method seems to be the best candidate to obtain B_1 maps, while actual flip-angle imaging method yields better B_1 maps than double angle method. To achieve the same SNR values with widely-used double angle method, averaging must be done for actual flip-angle imaging method and Bloch-Siegert shift based method. When acquisition times are selected equal for all, both Bloch-Siegert shift based method and actual flip-angle imaging method exceed double angle method by having SNR at least twice. From a different point of view, to achieve the same SNR, Bloch-Siegert shift based method requires less acquisition time in comparison to other mentioned methods (theoretically, one-tenth with comparison to double angle method and half with comparison to actual flip-angle imaging method).

For standard MREPT and cr-MREPT methods, the second phantom with anomalies is used. bSSFP magnitude and phase images are shown in Figure 4.8.

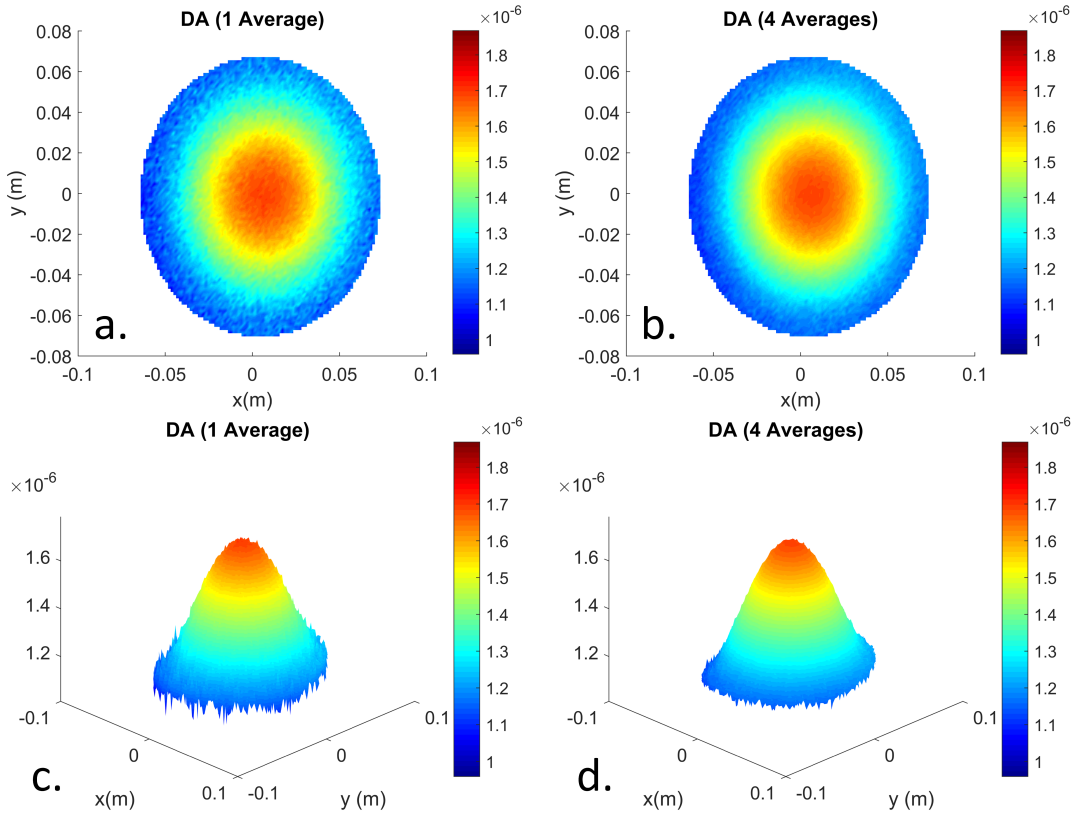

Figure 4.4: Experimental B_1 maps are taken by using double angle method. **(a)** B_1 map without any averaging, **(b)** B_1 map with 4 averages, **(c,d)** are the same as (a,b) and they are drawn as 3D surface plot.

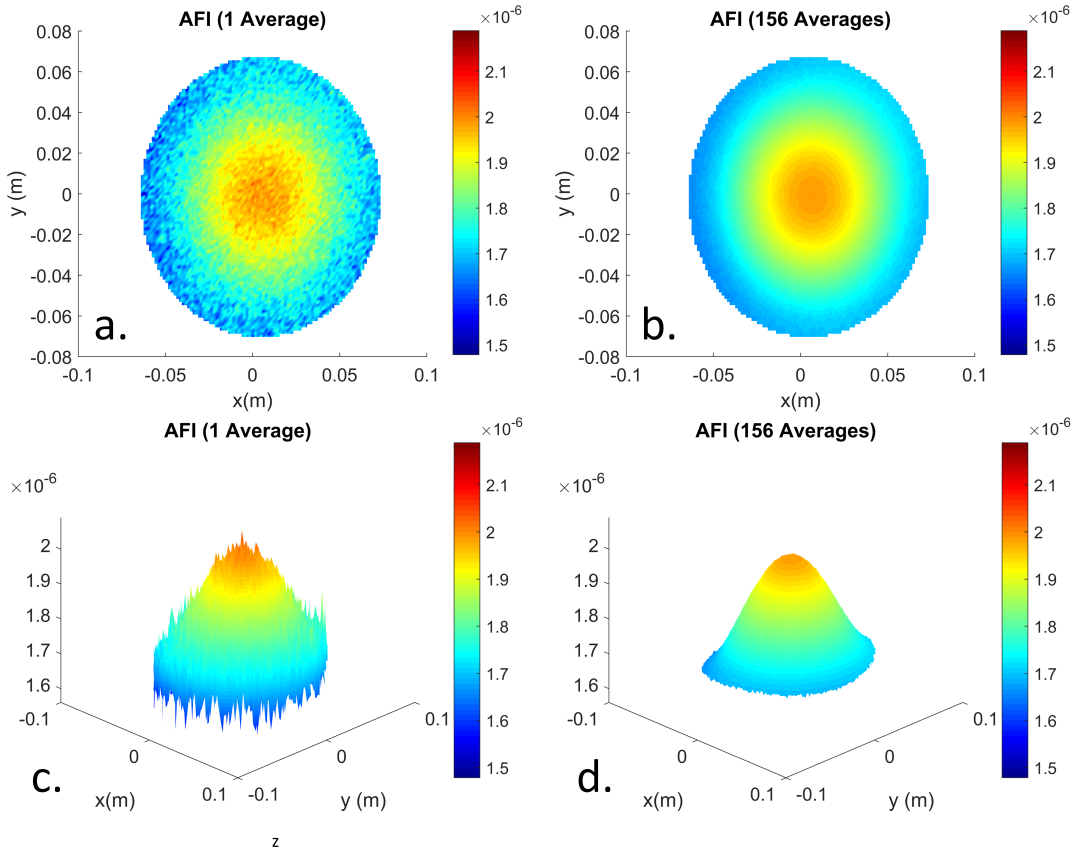

Figure 4.5: Experimental B_1 maps are taken by using actual flip-angle imaging method. **(a)** B_1 map without any averaging, **(b)** B_1 map with 156 averages, **(c,d)** are the same as (a,b) and they are drawn as 3D surface plot.

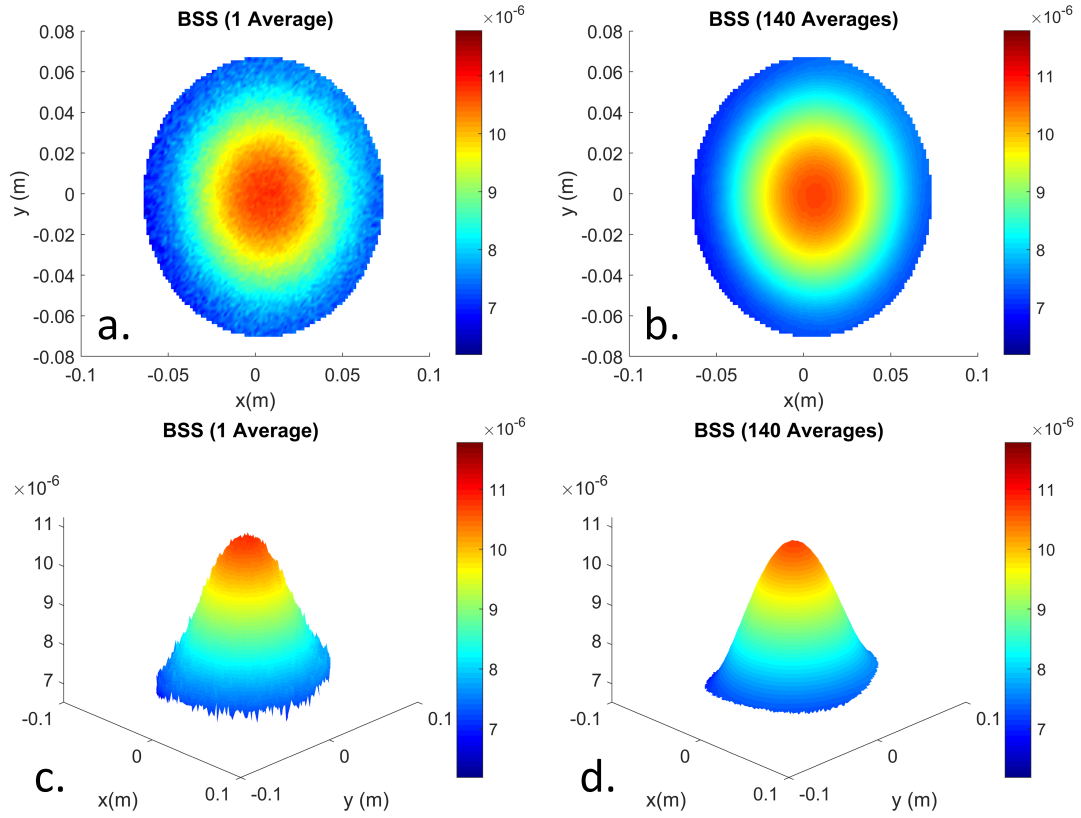

Figure 4.6: Experimental B_1 maps are taken by using Bloch-Siegert shift based method. **(a)** B_1 map without any averaging, **(b)** B_1 map with 140 averages, **(c,d)** are the same as (a,b) and they are drawn as 3D surface plot.

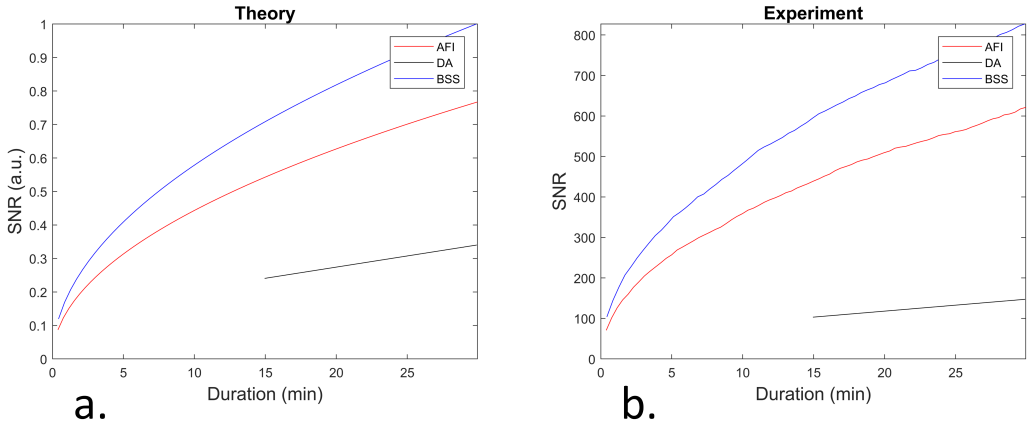

Figure 4.7: **(a)** Theoretical and **(b)** experimental comparison of SNR for double angle method (black line), actual flip-angle imaging method (red line) and Bloch-Siegert shift based method (blue line)

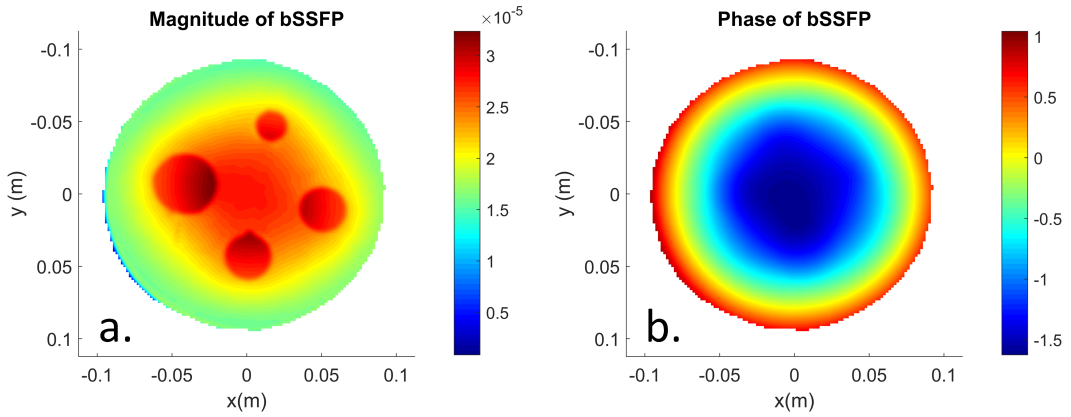

Figure 4.8: For the second phantom experiment, **(a)** magnitude and **(b)** phase of the bSSFP image are shown

Location of the anomalies can be seen in magnitude of the bSSFP image (Figure 4.8a) clearly. B_1 magnitude maps of this phantom is shown in Figure 4.9 for each method. Similar to the previous experiment, increasing the number of averages results less noisy B_1 magnitude maps as expected. Conductivity maps, which are obtained via standard MREPT method by using B_1 phase and magnitude, are shown in Figure 4.10 for each method. It can be noted that, although averaging increases SNR of the B_1 magnitude maps, it has a minimal effect on conductivity maps. Conductivity maps, which are obtained via cr-MREPT method by using B_1 phase and magnitude, are shown in Figure 4.11 for each method. It is clearly seen that averaging has beneficial effects on conductivity maps that are taken via cr-MREPT method. Also, visually, it can be seen that Bloch-Siegert shift based method is advantageous over actual flip-angle imaging method and double angle method.

4.5 Discussion and Conclusions

For SNR-wise, it is shown that, Bloch-Siegert shift based method yields high-SNR B_1 magnitude maps in comparison to actual flip-angle imaging method and double angle method. However, in this thesis, experiments are done for only

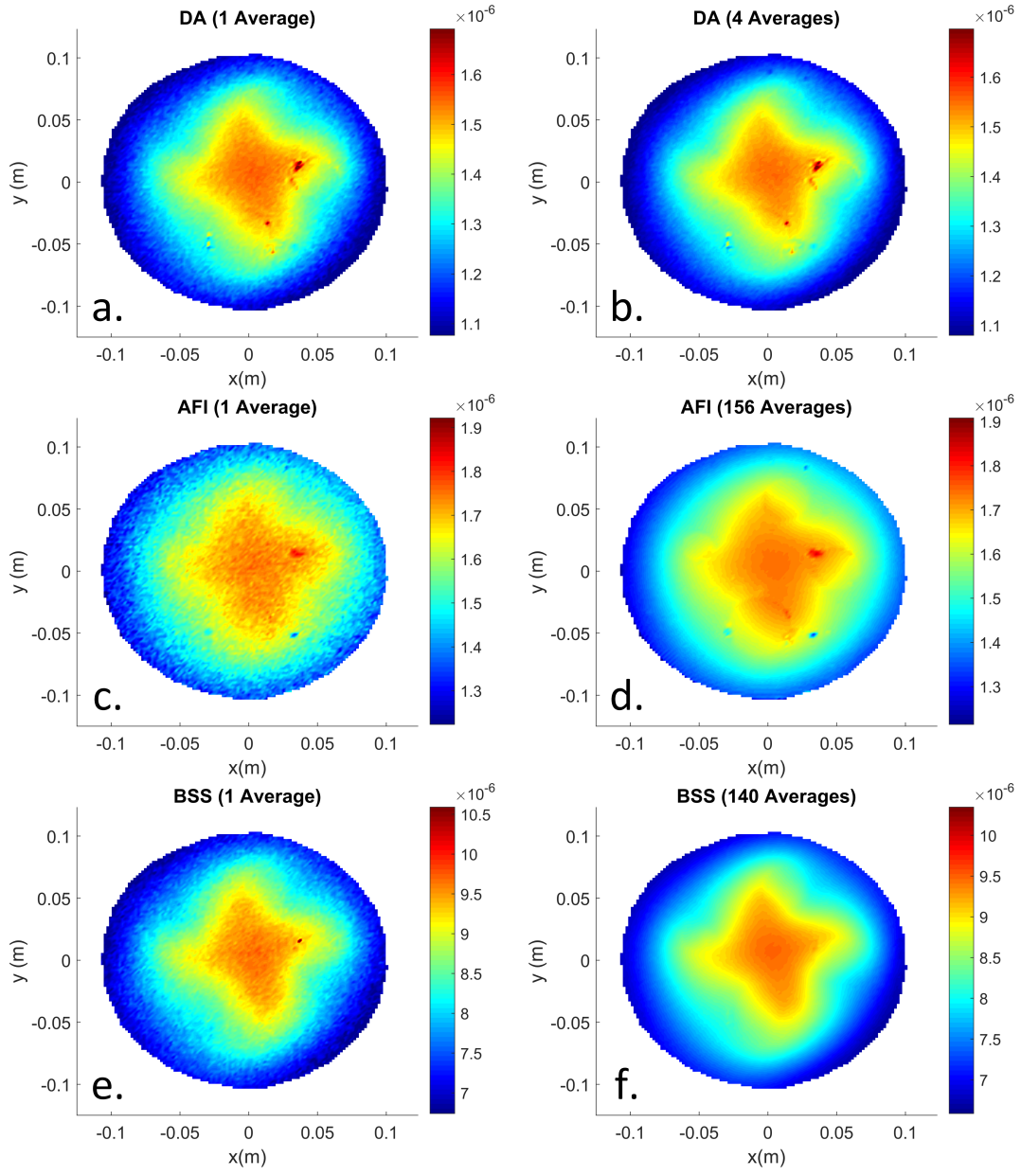

Figure 4.9: For phantom with anomalies experiment, B_1 maps which are obtained by using **(a,b)** double angle method, **(c,d)** actual flip-angle imaging method, **(e,f)** Bloch-Siegert shift based method with different number of averages are shown.

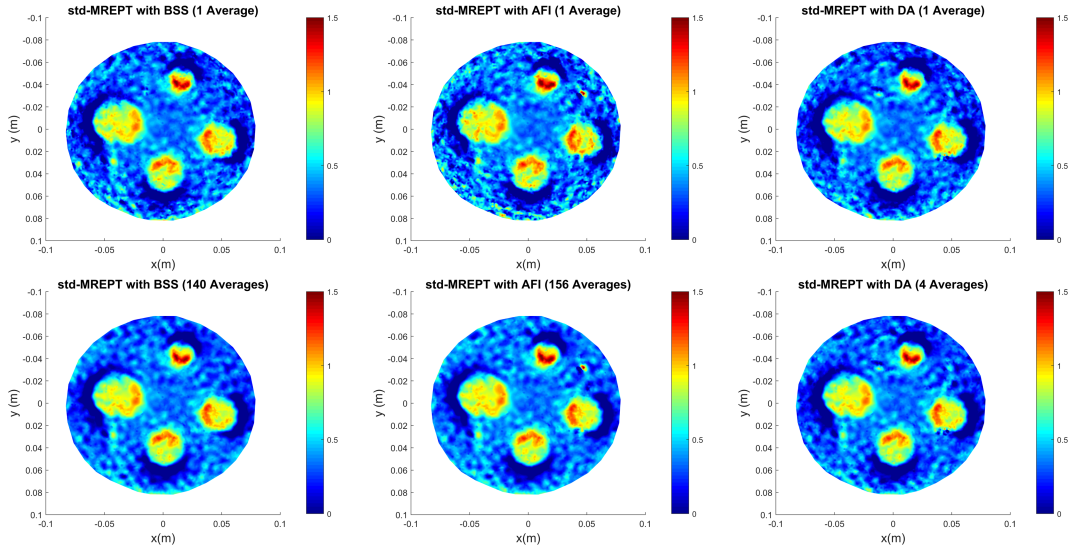

Figure 4.10: For phantom with anomalies experiment, conductivity maps which are obtained via standart MREPT method by using **(a,b)** double angle method, **(c,d)** actual flip-angle imaging method, **(e,f)** Bloch-Siegert shift based method with different number of averages are shown.

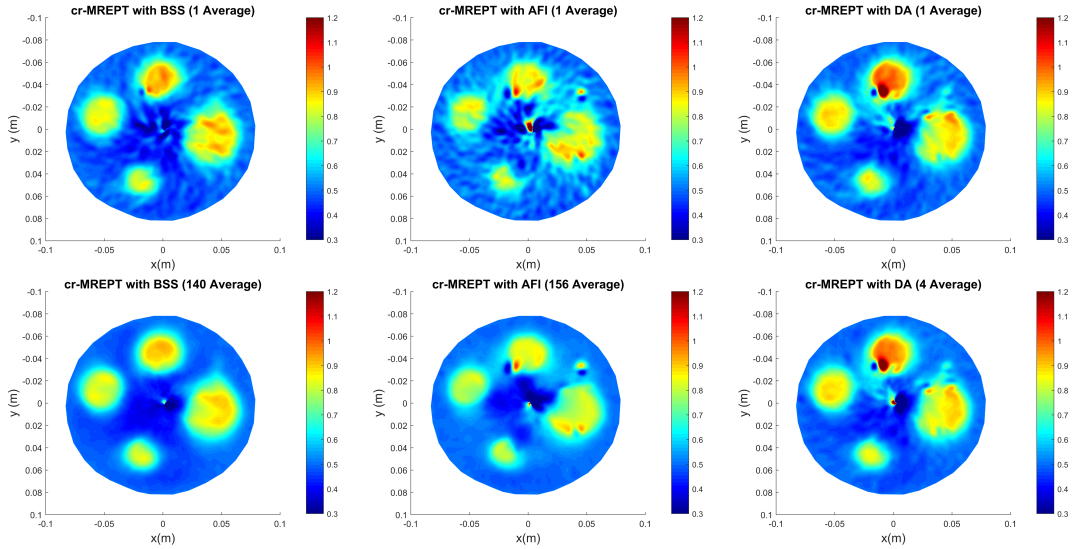

Figure 4.11: For phantom with anomalies experiment, conductivity maps which are obtained via cr-MREPT method by using **(a,b)** double angle method, **(c,d)** actual flip-angle imaging method, **(e,f)** Bloch-Siegert shift based method with different number of averages are shown.

one slice. With additional slice acquisitions, while scanning times for actual flip-angle imaging and Bloch-Siegert shift based methods increase linearly, scanning time for double angle method does not change. This is because gradient echo sequence, that is utilized in double angle method, uses multi-slice acquisition, and that allows the user to obtain more than one slice in one TR. Therefore, the choice of B_1 magnitude mapping method must be performed carefully.

Although taking averages and using better B_1 magnitude mapping techniques increase SNR, they do not affect conductivity maps, which are taken by using standard MREPT method, substantially. This is because, as known in literature, while permittivity is heavily based on B_1 magnitude, conductivity highly depends on B_1 phase [42]. However, for cr-MREPT method, it is clear that averaging is an important factor for obtaining accurate conductivity images.

Chapter 5

Conclusions

MREPT is considered as a potential diagnostic tool, because it provides the contrast between healthy and malignant tissues. It is also easy to implement, since MREPT does not require any additional hardware other than standard MRI system. To obtain electrical properties using MREPT, one needs both B_1 phase and magnitude. In this thesis, different approaches for acquisition of B_1 phase and magnitude is discussed.

bSSFP sequence is widely used to obtain B_1 phase, thanks to its numerous advantages, namely high SNR, high speed, motion insensitivity and automatic eddy current compensation. On the other hand, bSSFP suffers greatly from B_0 inhomogeneity and concomitant banding artifact. This problem prevents us to acquire accurate conductivity maps. In order to solve this issue, three different methods are implemented, namely inserting B_0 and T_2 information, linearization for off-resonance estimation - Gauss-Newton nonlinear search (LORE-GN) algorithm and PLANET method.

Inserting B_0 and T_2 information to the steady state bSSFP signal equation requires one B_0 map, one T_2 map and two bSSFP images with an excitation frequency difference. By using B_0 and T_2 values of each pixel, bSSFP phase is corrected and undistorted B_1 phase images are obtained. However, this method

requires B_0 and T_2 maps of the imaged object. When reliable and widely accepted B_0 and T_2 mapping methods are used, acquisiton time becomes high. For example, for phantom experiments, B_0 and T_2 mapping takes 15 minutes and 45 minutes, respectively. Since especially T_2 mapping requires long acquisition time, fast T_2 acquisition methods can be implemented to shorten the scanning time. For instance, multi-spin-echo sequence with the compensation technique for interfering stimulated echoes can be used [39]. Another fast T_2 mapping method, utilizing one single scan based on triple echo steady-state (TESS) sequence makes use of modelling the relation between the echoes and an iterative numerical solution for obtaining the T_2 map [40]. Motion insensitive rapid configuration relaxometry (MIRACLE) is similar to TESS and merges TESS with a balanced acquisition scheme [43]. All these methods can be used to decrease T_2 mapping to 5-10 minutes. However, they need to be carefully optimized for SNR and artifacts so that they are acceptable for MREPT. In addition to this, it can be argued that, correcting phase information is possible even with one bSSFP image with the help of T_2 and B_0 map using Equations 3.6 and 3.7. However, there is a fundamental drawback of Equations 3.6 and 3.7 for f_{OR} values close to the banding regions. In those regions, f_{OR} dependence of phase is very steep and therefore even a small error in the measured f_{OR} value would result in an overly erroneous phase value. To avoid these ill-conditioned regions of the magnetization versus off-resonance graphs, we have chosen to utilize two bSSFP runs and use the pass-band regions of either of them.

Although methods that are based on phase-cycled imaging offers huge advantages in acquisition time, one needs to use these methods carefully. For example, PLANET method uses elliptical signal model by using different phase-cycled images. By fitting pixel-wise complex valued points that are obtained from different phase-cycled images to an ellipse, B_1 phase can be obtained. However, PLANET method is susceptible to B_0 changes, like B_0 drift. During scanning, changes in B_0, for the points especially near the banding artifacts, distort the points that will be fitted on ellipse. Although, the shape of the ellipse will not change drastically, location of the points will be shifted on the ellipse. This phenomenon causes inaccurate B_1 phase images. Another problem related to PLANET method is

propagation of error. In PLANET method, B_1 phase is obtained in two steps. In the first step, T_1 map, T_2 map and banding-free magnitude images are found. Afterwards, B_0 map is acquired and it is used to obtain B_1 phase images. Note that B_1 phase can be obtained only through B_0 map. However, due to the error accumulation through each step, B_1 phases can be incorrect. Therefore, LORE-GN algorithm is considered advantageous over PLANET method, since it does not have such causes of distortion and takes less acquisition time (needs 3 phase-cycled bSSFP images, while PLANET method needs 6).

In order to obtain B_1 magnitude maps, double angle method, actual flip-angle imaging method, and Bloch-Siegert shift based method is used. According to theoretical SNR calculations and experimental SNR results, Bloch-Siegert shift based method is preferable over actual-flip angle imaging method and double angle method for single slice B_1 magnitude mapping. However, with acquisition of more than one slice, while total acquisition time of double angle method does not change, acquisition times of actual flip-angle imaging method and Bloch-Siegert shift based method change linearly with the number of slices. This is because double angle method utilizes gradient echo sequence which uses multi-slice acquisition (obtaining more than one slice in a single TR). Therefore, the most suitable B_1 magnitude mapping method should be determined based on theoretical SNR calculations and the number of slices.

It is shown that, for standard MREPT method, the choice of B_1 magnitude mapping method is not that important. This situation is consistent with the literature, since it is known that conductivity is mostly dependent on B_1 phase, while permittivity heavily depends on B_1 magnitude [42]. However, obtained results indicate that, for cr-MREPT method, B_1 magnitude maps with high SNR are required.

Bibliography

[1] A. J. Surowiec, S. S. Stuchly, J. R. Barr, and A. Swarup, "Dielectric Properties of Breast Carcinoma and the Surrounding Tissues," *IEEE Transactions on Biomedical Engineering*, vol. 35, no. 4, pp. 257–263, 1988.

[2] W. Joines, Y. Zhang, C. Li, and R. Jirtle, "The measured electrical properties of normal and malignant human tissues from 50 to 900 MHz," *Med Phys.*, vol. 21, no. 4, pp. 547–550, 1994.

[3] F Salinas, J Lancaster, and P. Fox, "3D modeling of the total electric field induced by transcranial magnetic stimulation using the boundary element method," *Physics in Medicine and Biology*, vol. 54, pp. 3631–3647, 2009.

[4] E Balidemaj, H Kok, and G. Schooneveldt"Hyperthermia treatment planning for cervical cancer patients based on electrical conductivity tissue properties acquired in vivo with EPT at 3 T MRI," *International Journal of Hyperthermia*, vol. 32, pp. 558–568, 2016.

[5] O Kwon, M Chauhan, and H. Kim "Fast conductivity imaging in magnetic resonance electrical impedance tomography (MREIT) for RF ablation monitoring," *International Journal of Hyperthermia*, vol. 30, pp. 447–455, 2014.

[6] U. Katscher, T. Voigt, C. Findeklee, P. Vernickel, K. Nehrke, and O. Dossel, "Determination of electric conductivity and local sar via b1 mapping," *IEEE Transactions on Medical Imaging*, vol. 28, no. 9, p. 1365?1374, 2009.

[7] D. C. Barber and B. H. Brown, "Applied potential tomography," *Journal of Physics E: Scientic Instruments*, vol. 17, p. 723, 1984.

[8] A. Mcewan, G. Cusick, and D. S. Holder, "A review of errors in multi-frequency eit instrumentation," *Physiological Measurement*, vol. 28, no. 7, 2007.

[9] H. Griffiths, "Magnetic induction tomography," *Measurement Science and Technology*, vol. 12, p. 1126, 2001.

[10] G. C. Scott, M. L. G. Joy, R. L.Ãrmstrong, and R. M. Henkelman, "Measurement of nonuniform current density by magnetic resonance," *IEEE Transactions on Medical Imaging*, vol. 10, pp. 362–374, 1991.

[11] Y. Z. Ider and O. Birgul, "Use of the magnetic field generated by the internal distribution of injected currents for electrical impedance tomography (MREIT)," *ELEKTRIK*, vol. 6, pp. 215–225, 1998.

[12] J. K. Seo, J.-R. Yoon, E. J. Woo, and O. Kwon, "Reconstruction of conductivity and current density images using only one component of magnetic field measurements," *IEEE Transactions on Biomedical Engineering*, vol. 50, pp. 1121–1124, 2003.

[13] Y. Z. Ider and S. Onart, "Algebraic reconstruction for 3D magnetic resonance electrical impedance tomography (MREIT) using one component of magnetic flux density," *Physiological Measurement*, vol. 25, p. 281, 2004.

[14] J. K. Seo, E. J. Woo, and O. Kwon, "Magnetic resonance electrical impedance tomography (MREIT): conductivity and current density imaging," *Journal of Physics: Conference Series*, vol. 12, p. 140, 2005.

[15] L. Özparlak and Y. Z. Ider, "Induced current magnetic resonance–electrical impedance tomography," *Physiological Measurement*, vol. 26, no. 2, 2005.

[16] E. M. Haacke, L. S. Petropoulos, E. W. Nilges, and D. H. Wu, "Extraction of conductivity and permittivity using magnetic resonance imaging," *Physics in Medicine and Biology*, vol. 36, p. 723?734, Jan 1991.

[17] H. Wen, "Noninvasive quantitative mapping of conductivity and dielectric distributions using rf wave propagation effects in high-field mri," *Medical Imaging 2003: Physics of Medical Imaging*, Sep 2003.

[18] J. Liu, Y. Wang, U. Katscher, and B. He, "Electrical properties tomography based on B_1 maps in MRI: Principles, applications, and challenges," *IEEE Transactions on Biomedical Engineering*, vol. 64, no. 11, p. 2515–2530, 2017.

[19] U. Katscher and C. A. V. D. Berg, "Electric properties tomography: Biochemical, physical and technical background, evaluation and clinical applications," *NMR in Biomedicine*, vol. 30, no. 8, 2017.

[20] F. S. Hafalir, O. F. Oran, N. Gurler, and Y. Z. Ider, "Convection-reaction equation based magnetic resonance electrical properties tomography (cr-mrept)," *IEEE Transactions on Medical Imaging*, vol. 33, no. 3, p. 777–793, 2014.

[21] J. Liu, X. Zhang, S. Schmitter, P. van de Moortele, B. He, "Gradient-Based Electrical Properties Tomography (gEPT): A Robust Method for Mapping Electrical Properties of Biological Tissues In Vivo Using Magnetic Resonance Imaging," *Magnetic Resonance in Medicine*, vol. 74, no. 3, p. 634–646, 2015.

[22] E. Balidemaj, C. A. V. D. Berg, J. Trinks, A. L. V. Lier, A. J. Nederveen, L. J. A. Stalpers, H. Crezee, and R. F. Remis, "Csi-ept: A contrast source inversion approach for improved mri-based electric properties tomography," *IEEE Transactions on Medical Imaging*, vol. 34, no. 9, p. 1788–1796, 2015.

[23] U. Katscher, D. H. Kim, and J. K. Seo, "Recent Progress and Future Challenges in MR Electric Properties Tomography," *Computational and Mathematical Methods in Medicine*, vol. 2013, p. 1–11, 2013.

[24] N. Gurler and Y. Z. Ider, "Gradient-based electrical conductivity imaging using MR phase," *Magnetic Resonance in Medicine*, vol. 77, p. 137–150, 2016.

[25] C. Stehning, T. R. Voigt, and U. Katscher, "Real-Time Conductivity Mapping using Balanced SSFP and Phase-Based Reconstruction," in *Proceedings of the 19th Annual Meeting of ISMRM*, (Montreal, Quebec, Canada), 2011.

[26] A. L. H. M. W. van Lier, D. O. Brunner, K. P. Pruessmann, D. W. J. Klomp, P. R. Lujiten, J. W. W. Lagendijk, and C. A. T. van den Berg, "B1 Phase

mapping at 7 T and its application for in vivo electrical conductivity mapping," *Magnetic Resonance in Medicine*, vol. 67, p. 552–561, 2011.

[27] A. L. H. M. W. van Lier, A. Raaijmakers, T. Voigt, J. J. W. Lagendijk, P. R. Lujiten, U. Katscher, and C. A. T. van den Berg, "Electrical Properties Tomography in the Human Brain at 1.5, 3, and 7T: A Comparison Study," *Magnetic Resonance in Medicine*, vol. 71, p. 354–363, 2013.

[28] M. Björk, R. R. Ingle, E. Gudmundson, P. Stoica, D. G. Nishimura, and J. K. Barral, "Parameter estimation approach to banding artifact reduction in balanced steady-state free precession," *Magnetic Resonance in Medicine*, vol. 72, no. 3, p. 880–892, 2013.

[29] Y. Shcherbakova, C. A. V. D. Berg, C. T. Moonen, and L. W. Bartels, "Planet: An ellipse fitting approach for simultaneous t1 and t2 mapping using phase-cycled balanced steady-state free precession," *Magnetic Resonance in Medicine*, vol. 79, no. 2, p. 711–722, 2017.

[30] R. Stollberger and P. Wach, "Imaging of the activeb1 fieldin vivo," *Magnetic Resonance in Medicine*, vol. 35, no. 2, p. 246–251, 1996.

[31] V. L. Yarnykh, "Actual flip-angle imaging in the pulsed steady state: A method for rapid three-dimensional mapping of the transmitted radiofrequency field," *Magnetic Resonance in Medicine*, vol. 57, no. 1, p. 192–200, 2006.

[32] L. I. Sacolick, F. Wiesinger, I. Hancu, and M. W. Vogel, "B1 mapping by bloch-siegert shift," *Magnetic Resonance in Medicine*, vol. 63, no. 5, p. 1315–1322, 2010.

[33] T. Voigt, U. Katscher, and O. Doessel, "Quantitative conductivity and permittivity imaging of the human brain using electric properties tomography," *Magnetic Resonance in Medicine*, vol. 66, no. 2, p. 456?466, 2011.

[34] D.-H. Kim, N. Choi, S.-M. Gho, J. Shin, and C. Liu, "Simultaneous imaging of in vivo conductivity and susceptibility," *Magnetic Resonance in Medicine*, vol. 71, no. 3, p. 1144–1150, 2013.

[35] S.-M. Gho, J. Shin, M.-O. Kim, and D.-H. Kim, "Simultaneous quantitative mapping of conductivity and susceptibility using a double-echo ultrashort echo time sequence: Example using a hematoma evolution study," *Magnetic Resonance in Medicine*, vol. 76, no. 1, p. 214–221, 2015.

[36] S.-K. Lee, S. Bulumulla, F. Wiesinger, L. Sacolick, W. Sun, and I. Hancu, "Tissue electrical property mapping from zero echo-time magnetic resonance imaging," *IEEE Transactions on Medical Imaging*, vol. 34, no. 2, p. 541–550, 2015.

[37] K. Scheffler, O. Heid, and J. Hennig, "Magnetization preparation during the steady state: Fat-saturated 3d truefisp," *Magnetic Resonance in Medicine*, vol. 45, no. 6, p. 1075–1080, 2001.

[38] P. Jezzard and R. S. Balaban, "Correction for geometric distortion in echo planar images from B0 field variations," *Magnetic Resonance in Medicine*, vol. 34, no. 1, p. 65-73, 1995.

[39] N. Ben-Eliezer, D. K. Sodickson, and K. T. Block, "Correction for geometric distortion in echo planar images from B0 field variations," *Magnetic Resonance in Medicine*, vol. 73, no. 2, p. 809-817, 2014.

[40] R. Heule, C. Ganter, and O. Bieri, "Triple echo steady-state (TESS) relaxometry," *Magnetic Resonance in Medicine*, vol. 71, no. 1, p. 230-237, 2013.

[41] G. R. Morrell and M. C. Schabel, "An analysis of the accuracy of magnetic resonance flip angle measurement methods," *Physics in Medicine and Biology*, vol. 55, no. 20, p. 6157–6174, 2010.

[42] S. B. Bulumulla, S. K. Lee, and D. T. B. Yeo, "Conductivity and permittivity imaging at 3.0 T," *Concepts in Magnetic Resonance Part B: Magnetic Resonance Engineering*, vol. 41B, no. 1, p. 13-21, 2012.

[43] D. Nguyen and O. Bieri, "Motion-insensitive rapid configuration relaxometry," *Magnetic Resonance in Medicine*, vol. 78, no. 2, p. 518-526, 2016.